DESIGN OF MAGNETIC TUMBLING MICROROBOTS FOR COMPLEX ENVIRONMENTS AND BIOMEDICAL APPLICATIONS

A Thesis

Submitted to the Faculty

of

Purdue University

by

Chenghao Bi

In Partial Fulfillment of the

Requirements for the Degree

of

Master of Science in Mechanical Engineering

December 2019

Purdue University

West Lafayette, Indiana

THE PURDUE UNIVERSITY GRADUATE SCHOOL
STATEMENT OF THESIS APPROVAL

Dr. David J. Cappelleri, Chair

    School of Mechanical Engineering

Dr. George T. C. Chiu

    School of Mechanical Engineering

Dr. Song Zhang

    School of Mechanical Engineering

Approved by:

    Dr. Jay P. Gore

        Head of the School Graduate Program

ACKNOWLEDGMENTS

First and foremost, I would like to thank Prof. David J. Cappelleri for his continuous support and guidance throughout this work. His insight was instrumental and he was the one who first opened my eyes to the exciting world of microrobotics.

I would like to thank Dr. Maria Guix for her amazing mentorship and assistance. Her positive attitude and past experience were greatly appreciated during the research process and the long nights at the lab. My labmates, especially Georges Adam, Benjamin V. Johnson, and Ze An, were always knowledgeable and enthusiastic. I will miss the many discussions we had and the time we spent working together.

I would like to thank my collaborators, including Elizabeth Neidert, Jiayin Xie, Elly Lambert, Prof. Craig Goergen, Prof. Nilanjan Chakraborty, and Prof. Luis Solorio for their contributions and biomedical/simulation help during this project. It would not have been possible without you.

I would like to thank Jesse Roll, Andrew Williams, Prof. Xinyan Deng, and Prof. Thomas Siegmund for their facilities and assistance in printing high-resolution 3D structures. I would like to thank Steve Florence for his help with lasercutting and machine shop guidance. I would also like to thank Mohammad Amin Karimi and Prof. Matthew Spenko for introducing and exploring the idea of 'gecko' adhesion.

I would like to express thanks to committee members Prof. Song Zhang and Prof. George T.C. Chiu for their patience and support, as well as the School of Mechanical Engineering for the financial support during my many years at Purdue.

Finally, I would like to thank my friends and family for all their encouragement and well wishes.

TABLE OF CONTENTS

LIST OF TABLES

LIST OF FIGURES

SYMBOLS

μ	friction coefficient
α	angle of robot's diagonal
B	external magnetic field strength
C	location of center of mass
f	friction force
f_{rot}	rotational frequency of magnetic field
F_a	adhesive force
F_{elect}	electrostatic force
H	height of robot
J	moment of inertia
L	length of robot
m	mass
M	magnetization of the robot
N	normal force
P	point on robot in contact with substrate
ϕ	alignment offset angle
r	half-length of diagonal
C	center of mass
v	translational velocity
V_m	magnetic volume
W	width of robot

ABBREVIATIONS

μTUM   microscale tumbling robot

DCP   differential complementarity problem

DOX   doxorubicin, an anticancer drug

ECP   equivalent contact point

MNCP   mixed nonlinear complementarity problem

MRI   magnetic resonance imaging

NdFeB   neodymium-iron-boron

NIR   near-infrared

NMP   N-methyl pyrrilidone

PBS   phosphate buffered saline

PDMS   polydimethylsiloxane

PLGA   poly(lactic-co-glycolic acid)

ABSTRACT

Bi, Chenghao M.Sc., Purdue University, December 2019. Design of Magnetic Tumbling Microrobots for Complex Environments and Biomedical Applications. Major Professor: David J. Cappelleri, School of Mechanical Engineering.

The mobility and biomedical applications of a microscale magnetic tumbling (μTUM) robot capable of traversing complex terrains in dry and wet environments is explored. Roughly 800 x 400 x 100 μm in size, the robot is fabricated using standard photolithography techniques and consists of a rectangular polymeric body with embedded NdFeB particles. Static force analysis and dynamic modeling of its motion characteristics are performed with experimental verification. Techniques for simulating the intermittent, non-contact behavior of tumbling locomotion are used to find an optimized design for the microrobot, reducing time and resources spent on physical fabrication. When subject to a magnetic field as low as 3 mT, the microrobot is able to translate at speeds of over 30 body lengths/s (24 mm/s) in dry conditions and up to 8 body lengths/s (6.8 mm/s) in wet conditions. It can climb inclined planes up to 60° in wet conditions and up to 45° in dry conditions. Maximum open loop straight-line trajectory errors of less than 4% and 2% of the traversal distance in the vertical and horizontal directions, respectively, were also observed. Full two-dimensional directional control of the microrobot was shown through the traversal of a P-shaped trajectory. The microrobot's real-time position can be accurately tracked through visual occlusions using ultrasound imaging. When applied as a coating, a fluorescein payload was found to diffuse over a two hour time period from the microrobot. Cytotoxicity tests also demonstrated that the microrobot's SU-8 body is biocompatible with murine fibroblasts. The microrobot's capabilities make it promising for targeted drug delivery and other *in vivo* biomedical applications.

1. INTRODUCTION

In the last two centuries, the average human lifespan has more than doubled from ∼29 years in 1800 to ∼71 years in 2015 [1, 2]. Advances in technology, economic equality, medicine, and medical procedures have played an enormous role in this increase, but there continues to be room for improvement. Though significant countermeasures have been built for the prevention and treatment of epidemic-prone infectious diseases such as HIV and malaria, tackling noncommunicable diseases (NCDs) remains a critical issue. These include most heart diseases, most cancers, diabetes, and chronic respiratory diseases. The World Health Organization estimates that 40.5 million people died from NCDs in 2016, or 71% of all total deaths that year [3]. Risk factors for NCDs have increased in the modern world, with more people becoming overweight or obese, leading sedentary lifestyles with less physical activity, eating foods with high calories and low nutrient levels, and continuing to consume tobacco and alcoholic products. Though many diagnosis and treatment methods for NCDs are available, they are often expensive and invasive, with less than optimal success rates and often lasting side effects. In the case of cancer, for example, radiation therapy and chemotherapy cause damage to surrounding tissues and can result in systemic toxicities [4]. A widely used chemotherapy drug, doxorubicin (DOX), is cardiac toxic and can lead to congestive heart failure after several years [5]. Additionally, these types of treatments cannot penetrate the blood-brain barrier and have difficulty reaching hypoxic areas in the body. While surgery can remove large portions of tumors and reduce symptoms immediately, it can also adversely affect the patient's quality of life, miss stray tumor cells, and damage otherwise healthy tissue to reach the tumor area [4]. There is an ongoing need to develop better methods to effectively diagnose and treat NCDs as they become increasingly prevalent in the future.

Rapid global industrialization has also led to worsening pollution in the environment. The amount of pesticide waste, heavy metal contaminants, air pollution, and organic/inorganic solvents in the environment grows every day. These pollutants have resulted in increased rates of cancer and respiratory problems in many parts of the world. Additionally, pathogenic microorganisms such as bacteria, viruses, and algae continue to release toxins that can cause various illnesses and diseases. Detection and quantitative analysis of these harmful substances in food, water sources, and populated living areas remains an important issue. Conventional methods of detecting toxic substances, such as liquid chromatography and nuclear magnetic resonance, are able to detect trace amounts and are highly reproducible [6, 7]. However, they also require advanced, costly equipment, extensive sample purification, and trained operators. A low-cost solution that can not only detect, but also break down these toxic substances would be the ideal way forward.

The relatively new field of microrobots, untethered machine systems smaller than a millimeter in size, will play an increasingly larger role in addressing these problems and improving human health overall. Formally speaking, a microrobot is "a programmable machine with partly or fully self-contained capabilities for mobility, sensing, and operation of predefined tasks" [8, 9]. Recent advancements in microelectronics and microfabrication have led to rapid growth in the design, performance, and potential of these machines, paving the way towards practical applications. Due to their diminutive size, microrobots have unprecedented access to areas inside the human body, bringing along motion control and advanced capabilities with them. They have the potential to perform tasks such as targeted drug delivery, tissue biopsies, microsurgery, and toxin detection/removal, while being minimally invasive and precise. A myriad of propulsion mechanisms, motion behaviors, fabrication techniques, and applications have already been experimentally demonstrated in recent literature. This diversity in robot designs is largely due to the significant advantages and disadvantages between each potential design choice, limiting most microrobots to exhibit optimal behavior in only a few applications or environments. While health practition-

ers may soon have a vast arsenal of robotic tools to address each specific problem, a single robot platform with diverse functionalization and the ability to address a variety of problems would be ideal.

There are many challenges facing robots in the small scale. Conventional electronics and hardware cannot fit on microscale objects without sacrificing mobility and size constraints. Because they are too small to incorporate batteries or traditional power sources, microrobots typically find power through other means, including fuel-based methods, such as chemical or biochemical propulsion, and external field-based methods, such as propulsion using light, ultrasound, magnetic, or thermal fields. Random Brownian motion and the increased effect of area-proportional forces (e.g. friction, adhesion, surface tension, etc.) make precise motion control difficult and require unconventional actuation methods to overcome. Creative fabrication methods must be devised to make complex geometry in the small scale and combine living organisms with synthetic parts. The result of these challenges is a rich research field with many new developments waiting to be discovered, a field that requires a multidisciplinary effort involving mechanical, chemical, medical, and material design.

To address one of the more critical problems, this thesis explores a versatile new method of microscale locomotion - magnetic tumbling - and evaluates its ability to overcome the difficult terrains and environments present within and beyond the human body, as well as explore the potential biomedical applications of a tumbling magnetic microrobot. In Chapter 2, the existing body of microrobot designs and applications are discussed in detail. Chapter 3 goes into the design of the magnetic tumbling robot, its fabrication method, and its design variations. Chapter 4 discusses the equations of motion used to describe the tumbling motion and presents a novel simulation method for predicting the robot's dynamic behavior. Finally, Chapter 5 and 6 detail the results of mobility characterization experiments and biomedical application experiments, respectively.

2. BACKGROUND AND RELATED WORK

Having the capability to self-propel and perform controllable navigation, microrobots are highly viable for targeted drug delivery applications, where the therapeutic efficacy of drugs is improved by reducing systemic side effects. Additionally, microrobots provide "protection for cargo" and "a high volume/surface for drug loading" [10]. Unlike passive drug diffusion alone, they also can deliver individual cells to desired locations to repair damaged tissue and restore organ functionality. They have the potential to perform intracellular DNA delivery and sensing operations. Personalized microrobots might even be made from a patient's own cells, in which they can "readily escape from the immune system and provide enhanced biocompatibility and biodegradeability" [10]. As described earlier in Chapter 1, the diverse functionalities possible for microrobots will allow them to meet a large variety of demands and applications. The refining and experimentation process typically begins in a test tube setting, then moves to the cellular level, before finally finishing with tests involving live animal models.

Critical factors in microrobot design include material properties and the method of propulsion and actuation. "The surface chemistry of micro[robots] has a significant influence on [their] physiochemical properties" and "through tailoring the surface groups the surfaces can be modified to act as the reaction sites, which [play] a very crucial role in dominating the interaction of micro[robots] with various analyte molecules in the environment" [11]. The surface properties also effect how pharmaceuticals are stored, retained, and released. The methods of propulsion and actuation used largely determine what environments a microrobot can operate in, how biocompatible it is, and what the limitations of its design will be.

2.1 Challenges

As scale shrinks down to the microscale levels, many challenges emerge that impede locomotion and precise control. Traditional methods of robot control and actuation are often infeasible at this scale and alternative methods must be used instead. Size constraints limit on-board power and computational ability. Few mobile microrobots, if at all, contain parts such as circuit boards and electric motors. Control is off-loaded instead to remote, off-board computers, using real-time feedback from visual, ultrasound, or X-ray imaging tools to manipulate the microrobot accordingly through external fields.

At the microscale and below, inherent Brownian motion and random variations on surface topology start to have a significant impact on locomotion. It becomes harder to maintain motion control and speed regulation than in the macroscale, where environmental properties tend to be more uniform. Here, surface properties can vary relatively significantly from one point to another, leading to highly stochastic environments that are difficult to perform measurements on. Unlike macro-scale applications, where water and air tend to be the only mediums that robots are intended to move through, there may also be highly viscous biological fluids that microrobots will have to negotiate.

Surface-area effects decrease quadratically as size decreases while volumetric effects decrease cubically. This relationship means that surface-area based effects such as friction, adhesion, and surface tension have a significantly higher impact at the microscale than they do at the macroscale, needing to be considered in dynamic modeling and robot design. Meanwhile, volumetric effects such as weight, inertia, and magnetic attraction have a reduced impact at the microscale. The combination of reduced inertia and higher relative viscosity (resulting in low Reynolds numbers) means that many forms of macroscale locomotion in fluids at the microscale will not work. The scallop theorem proposes that any kind of reciprocal motion, or motion that is identical viewed forward and backwards in time, would result in no net for-

ward motion in the microscale [12]. A scallop moves by opening its shell and closing it quickly, using the momentum of the expelled water to propel itself forward. In the microscale, the scallop would move backwards upon opening its shell and forwards to its original position after closing its shell, resulting in no net forward motion. Swimming at this size scale requires non-reciprocal motion or thrust that can only be achieved through flagella/cilia beating, bubble expulsion, corkscrew motion, etc.

A medical setting presents additional challenges as well. Unlike a controlled manufacturing setting, organic environments are highly complex and unpredictable, with many variable environmental properties that may change over time. A single organ can contain locations that are wet, dry, smooth, and sticky. Though arteries and capillaries offer a convenient way for blood to travel around the body, it is very difficult for small microrobots to move against the fluid flow within them. The robots must be inserted somewhat close to the point of interest and/or in mediums that are mostly static. Biocompatibility is another concern that limits what materials can be used to make the microrobots. Toxic metals and chemicals cannot be used inside the body and adverse reactions with the immune system should be avoided. If the microrobot cannot be extracted from the body after it is finished with its operation, it needs to be able to decompose into harmless, soluble nontoxic substances.

2.2   Propulsion Methods

Methods of propulsion and actuation of microrobots can largely be classified into two categories: fuel-based and external field-based. In fuel-based propulsion, the energy for movement either comes from fuel/energy stored within the microrobot itself or from a chemical reaction with the surrounding environment. In external field-based propulsion, the energy for movement comes from a field generator outside of the immediate environment that results in fuel-free actuation.

2.2.1 Chemical, Biochemical, and Biohybrid Propulsion

Chemical propulsion is a fuel-based propulsion method that relies on asymmetric chemical reactions around the microrobot for movement. This is typically done by creating tubular microrobots with a chemically reactive interior that can expel bubbles in a singular direction or by creating Janus particles that have surfaces with two or more distinct properties. These microrobots are generally composed of two sections: an inert material for structural support and a catalyst/active metal for triggering chemical reactions.

The most widely used fuel for synthetic chemical microrobots is H_2O_2, or hydrogen peroxide, due its ability to demonstrate higher motion speeds compared to other fuels. It can be found in biological systems as a short-lived byproduct in biochemical processes. Movement using H_2O_2 is possible using self-phoretic and bubble-driven mechanisms, with the latter showing higher speeds. Sen et al. fabricated Au-Pt bimetallic rods that moved autonomously in an H_2O_2 solution through self-electrophoresis [13]. The solution oxidized into O_2 preferentially at the Pt end compared to the Au end and resulted in a weak driving force forward, propelling the 1 μm rods to speeds of up to 10 μm/s [13]. Alternatively, Wang et al. synthesized bilayer polyaniline/Pt tubular microrobots that are propelled by recoil forces from the ejection of O_2 bubbles formed from reactions with the Pt interior [14]. Speeds of the 8 μm tube can reach over 2,800 μm/s while still operating at levels of H_2O_2 as low as 0.2% [14]. H_2O_2 at high concentrations, however, exhibits strong oxidation and is toxic to living organisms. Therefore, alternative fuels must be found for practical applications for chemical microrobots in biological systems.

Naturally occurring biological substances that can be used as fuel sources include urea, water, stomach acid, and glucose. Hollow mesoporous Janus nanorobots with embedded enzymes have been shown by Sánchez et al. to move using urea or glucose through a chemophoretic mechanism [15]. The reaction of active metals, such as magnesium, with water can also create hydrogen bubbles that can propel mi-

crorobots [16]. Wang et al. demonstrated tubular zinc microrockets with an inert polyaniline structure that can interact with highly acidic environments to generate O_2 bubbles for propulsion [17]. Though promising, issues with current chemically catalytic microrobots include weak driving forces, inability to operate in high ionic strength environments, short lifetimes, and harsh reaction conditions [18]. Moreover, the uncontrolled motion trajectory of many of these robots makes navigation difficult without the presence of external fields for additional control [11].

It can be advantageous to integrate living microorganisms with synthetic components in biohybrid microrobot designs. Bacteria and sperm cells are compliant, motile, energy-efficient, responsive to external stimuli, and biocompatible. They can propel themselves in biological environments with hair-like flagella or cilia structures. These flexible structures can either beat in a non-reciprocal motion or for some flagella specifically, rotate in a corkscrew-like motion using a molecular motor at the base of the flagella. Energy comes from the flow of charged ions, such Na^+ or H^+ ions, over the outer membrane of the organism and the conversion process between this chemical energy to kinetic energy is highly efficient. Sanchéz et al. demonstrated that *E. Coli* bacteria attached to iron-capped Janus particles were able to be guided by external magnetic fields and could carry particle cargo. Similarly, Felfoul et al. controlled a magnetotactic bacteria species, *Magnetococcus sp.*, into penetrating a solid *ex vivo* tumor [19]. Magnetotactic bacteria species "tend to swim along [magnetic field] lines and toward low O_2 concentrations based on a two-state aerotactic sensing system" [18]. This makes them advantageous for targeting cells in hypoxic areas of the body while still maintaining steering control through external magnetic fields. Magdanz et al. were able to trap living bovine sperm cells in magnetic microtubes [20]. The individual sperm cells encapsulated by the magnetic microtubes provided forward propulsion while again, an external magnetic field controlled the direction of motion [21]. The primary disadvantage to biohybrid microrobot designs is that the robots must always be kept in an environment that allows for the survival of the microorganism, containing proper nutrients and the correct physiological con-

ditions. Additionally, it is still uncertain how the inclusion of therapeutic payloads into living organisms affects their biological functionality.

2.2.2 External Field Propulsion

Energy for propulsion can come from external stimuli to power fuel-free microrobots. This external stimuli comes in many forms, including light, electric, ultrasound, and magnetic fields.

External light sources can be used to trigger "photocatalytic reactions, photoisomerization, and photothermal conversions" in photoactive materials [18]. These effects can be taken advantage of for propulsion and drug release mechanisms. Zhang et al. used UV light to generate O_2 molecules on the illuminated surface of a TiO_2 microrobot, propelling the robot towards areas with low O_2 concentration [22]. Abid et al. used reversible isomerization of azobenzene to change its material properties and the resultant surface tension gradients were able to generate motion in an azobenzene-coated microrobot [23]. Thermal gradients created from pointing continuous near infrared laser irradiation on gold nanoparticles resulted in ultrafast movement in water [24]. A similar technique was used to perform thermal ablation of tumor cells [25]. Light-powered microrobots are "easy [to] manuever" and have a "fast response", but the hydrogen peroxide used to form O_2 is not biocompatible, "strong laser power can cause damage to biological samples", light requires an unimpeded line of sight to the target, and "UV light cannot penetrate deeply" into tissue [18].

Electrically driven microrobots are made from "materials with a dielectric mismatch with the environment" and work using electro-osmotic effects, "electrokinetic effects, electrically triggered chemical reactions, and electric tweezers" [18]. Fan et al. demonstrated that gold nanowires can be manipulated by electric tweezers and delivered to a target cell. The wires were functionalized by coating them in tumor-necrosis factor-alpha (TNFα) [26]. A more advanced version of the nanowires was created by splitting nanoparticles into three separate sections (Au-Ni-Au) that allowed for the

controlled rotation speed of the nanorobots, changing the drug release rate from the particles [27]. The main drawbacks of electric field actuation are that it can be sensitive to the ionic strength of the surrounding fluid, it can require high voltages, and it can require large semiconductor diodes and conductive beads to operate, making it unsuitable for *in vivo* applications within the body.

Ultrasound fields are advantageous because they are non-invasive, can deeply penetrate biological tissue, and can propel microrobots in high viscosity environments [18]. Ultrasound standing waves in the MHz frequency range were shown by Wang et al. to be able to "levitate, propel, rotate, align, and assemble" bimetallic microrods in both highly viscous and highly ionic fluids in a controlled environment of limited size [28]. The exact actuation mechanism remains unknown, but it is proposed that this fast motion, which only occurs in certain positions, is due to the shape asymmetry of the rods and their higher density (and as a result, higher inertia,) than the surrounding fluid [28]. The same research group also demonstrated superfast ultrasound-propelled microtubes, using high frequency ultrasound waves to vaporize perfluorocarbon droplets trapped within the tubes to produce ejected gas bubbles [29]. These bubbles propelled the tubes to almost bullet-like average speeds of 6 m/s, allowing the tubes to cleave through tissue and deeply embed themselves inside [29]. Red blood cells were functionalized with Fe_3O_4 nanoparticles by Li et al. to produce highly biocompatible microrobots [30]. The asymmetry of the nanoparticle distribution inside and the red blood cells themselves resulted in a significant net propulsive force when the cells were subjected to ultrasound waves. The embedded magnetic nanoparticles allowed for additional steering and guidance using external magnetic fields. Red blood cell microrobots can pass through biological barriers easily and are viable for a variety of practical biomedical applications, including usage as toxin sponges or drug carriers. The difficulty lies in functionalizing the cells without damaging their outer membranes too much and compromising their unique properties.

Similar to ultrasound fields, magnetic fields are non-invasive and harmlessly penetrate biological tissue. As demonstrated by clinical applications of magnetic resonance

imaging (MRI) machines, magnetic fields of strength higher than 5 Tesla (T) can be used safely on patients. Though extreme field strength magnitudes and rapid changes in field strength can result in excessive heating of the tissue, it is unlikely that dangerous limits will be reached in practical usage. A study by J. Schenck concluded that any static magnetic field less than 8 T in strength is safe for human use [31]. The two ways a magnetic field can influence a magnetic object are force induced through spatial field gradients and torque induced through differences in magnetic field polarization. Magnetic objects are pulled toward regions with greater magnetic flux density and also experience a magnetic moment when their polarization does not align with that of the external field. The time-varying changes in external field gradients, strength, and polarization result in net forward motion of the magnetic object. Because magnetic force through spatial gradients scales volumetrically while magnetic torque scales by length, torque-based magnetic robots are generally preferred at the microscale due to their higher efficiency. This is especially important for biomedical applications, where the strength of the magnetic field decreases rapidly over distance and it may not be possible to place the field source extremely close to the microrobot. These robots typically contain magnetic materials such as iron oxide (Fe_2O_3, Fe_3O_4), nickel (Ni), and neodymium-iron-boron (NdFeB) to allow them to be manipulated by the external magnetic fields.

Generally, magnetic microrobots can be divided into two categories: swimmers and surface walkers. Magnetic swimmers are propelled using both stiff and flexible artificial flagella. Generally, magnetic swimmers using stiff, helical flagella tend to achieve higher speeds with more precise steering control. Though less efficient, microtubes and nanorods have also been manipulated in wet media using magnetic force gradients [21, 32]. Dreyfus et al. demonstrated flexible flagella microrobots powered through oscillating fields. The flagella were made from a series of superparamagnetic beads linked together with DNA and attached to individual red blood cells at the end of the chain [33]. Under a transverse oscillatory magnetic field, a bending wave propagated along the filament of beads and propelled the robot forward. Stiff, nickel-

coated helical microrobot structures have also been demonstrated in multiple studies, propelling themselves through fluid mediums using corkscrew action under a rotating, uniform magnetic field. Nelson et al., for example, demonstrated 3D navigation of these helical swimmers under low-strength, rotating magnetic fields to deliver plasmid DNA to human embryonic kidney cells [34].

To tackle of the issue of moving through dry media, many magnetic surface walker variants have been developed. Unlike swimming, surface locomotion requires physical contact with a solid surface to work and is restricted from full spatial movement in three dimensions. It can be advantageous, however, because a variety of surface locomotion methods work in both wet and dry environments. Sitti et al. created a block-like NdFeB microrobot that took advantage of stick-slip motion to move at controllable speeds of up to 2.8 mm/s, though the robot was observed to move at speeds faster than 10 mm/s [35, 36]. This speed was achievable through the constant rocking and sliding motion of the magnetic microrobot at high frequencies over a flat surface. Hou et. al experimented with tumbling and rolling locomotion under a external rotating magnetic field using a rectangular stainless steel microrobot and an iron wire microrobot encapsulated by a spherical UV adhesive shell [37, 38]. These microrobots were capable of speeds of 1.4 mm/s and 13.2 mm/s respectively in dry air. The same rolling motion was shown by Nelson et. al to be capable of creating vortices in wet media that could transport protein crystals without direct physical contact and risking damage to them [39]. The "MagMite" and "PolyMite" successor designs use inertia- and impact-driven mechanical force to propel themselves controllably over flat surfaces in both wet and dry media [40–42]. Incorporating an on-board hammer and spring system, the microrobots impart a large output force and were capable of pushing microobjects such polystyrene and glass beads in water. More recently, Sitti et al. developed soft magnetic millirobots capable of multimodal locomotion [43]. These flexible polymer robots have non-uniform magnetic alignment and can "swim inside and on the surface of liquids, climb liquid menisci, roll and walk on solid surfaces, jump over obstacles, and crawl within narrow tunnels" in addition

to performing "pick-and-place and cargo-release tasks" [43]. Though they have a dizzying array of capabilities, the fabrication process for these robots has yet to be miniaturized to the microscale.

2.3   Biomedical Applications

There are myriad of potential biomedical applications for micro-/nanorobots and investigation into many of these applications has already begun. Examples range from intracellular DNA delivery to tissue biopsies [21,44]. In addition to incorporating physical actuation and release mechanisms, the external surface of micro-/nanorobots are often functionalized with a variety of components, since this is the part that directly interacts with exogenous substances.

Many microrobots in literature focus on the application of targeted drug delivery specifically. The basic requirements for targeted drug delivery are relatively simple, requiring only controllable locomotion within the body and a way to store and release the desired drug. There are several challenges with conventional drug delivery, where the drug passively diffuses to a target location. Due to the off-target drug distribution, this strategy often requires high dosages and repeated administration to guarantee efficacy. The off-target distribution combined with the repeated high dosages can result in severe side effects. Additionally, drugs often have short half-lives and are rapidly cleared from the body. By using nanoliposomal formulations of existing passive drug systems, medical scientists were able to increase circulation time and enhance the drug permeation and retention effects. These improvements, however, have yet to result in a strong clinical response. "Over 95% of [the] administered nanocarriers still appear[ed] in other organs and [brought] about serious side effects" [18]. Additionally, the use of nanocarriers alone also does not solve the problem of penetrating biological barriers.

Microrobots can actively target individual cells for the delivery of drugs and therapeutics, while being able to protect them from degradation and potentially traverse

through biological barriers at the same time. Avila et al. wrapped gold nanowires with interfering RNA strands for accelerated intracellular delivery [45]. The wires were propelled using ultrasound waves and resulted in 94% gene silencing of targeted tumor cells, about a 13-fold improvement in silencing response compared to static modified nanowires. Similarly, Bruhn et al. showed an increase of 50% in cell gene knockout when ultrasound-powered nanomotors were used instead of static nanowires [46]. Ko et al. demonstrated a soft, magnetically-propelled microrobot that unfolded as the surrounding acidity of the environment decreased, reducing the viability of mammary carcinoma cells by 70% with its cancer microbead payload [47]. Peng et al. functionalized stomatocyte nanomotors, bowl-shaped red blood cells without nuclei, that autonomously moved towards hydrogen peroxide-secreting neutrophil cells after it was observed that stomatocytes naturally move in a particular direction in the presence of a fuel gradient [48]. Ultrasound-driven porous nanowires were used by Wang et al. to significantly increase payload size and deliver DOX to cancer cells [49]. NIR light resulted in controlled release of the drug payload via photothermal effects. 'Smart' carriers have also been developed using liposomes, spherical sacs of phospholipid molecules encapsulating an aqueous drug solution. These drug-loaded liposomes only release when the liposomes fuse with the specifically targeted cell membrane or through endocytosis [50]. In addition to liposomes, sperm cells used in motile biohybrid microrobot designs can fuse with tumor cells as well [51]. Avila et al. demonstrated one of the first *in vivo* applications of microrobots by treating gastric bacterial infections in mice with drug-loaded magnesium micromotors [52]. The pH-sensitive payload was released after the tube's outer layer neutralized the surrounding stomach acid. Li et al. observed that motile bacterial drug carriers showed DOX accumulations *in vivo* of "12.9% of the injected doses per gram of tissue" three hours after the carriers were injected, which is "much higher than commonly used nanocarriers" [53]. Functionalized neutrophils, the most common type of immune cell, were shown by Zhang et al. to be capable of penetrating the brains of live mice and suppressing the recurrence of glioma tumors [54]. This capability may prove use-

ful in treating other brain disorders such as multiple sclerosis and Alzheimer's disease in the future.

Microrobots can also be used for imaging applications and identifying varying substances throughout the body. Yan et. al fabricated helical microswimmers from *Spirulina* microalgae by coating them in magnetite (Fe_3O_4) suspensions. The natural properties of the microalgae made them visible *in vivo* using fluorescence imaging while magnetic resonance imaging was able to track a swarm of these microswimmers inside deep locations within the rodent stomach that fluorescence-based imaging could not penetrate [55]. A hydrogel-based biodegradable microswimmer was demonstrated by Ceylan et al. to swell in the presence of cancer marker MMP-2, releasing the magnetic nanoparticles used for propulsion in the vicinity of breast cancer cells. This effect realizes the potential of marking target local tissue sites for medical imaging after therapeutic intervention [56]. The outer layer of a microrobot can be functionalized with boronic acid to allow for recognition of sugar, endotoxins, and bacteria [57]. When combined with carbon dots or semiconductor quantum dots (nanoparticles that can be observed using fluorescent probes), the resulting microrobots act as ultrafast sensors for detecting harmful bacterial endotoxins [58]. Vilela et. al used chemisorption of an iodine isotope onto a micromotor's gold surface to enable positron emission tomography (PET) tracking of a swarm of micromotors through opaque surfaces using existing medical imaging technology [59]. High-resolution ultrasound imaging is also capable of detecting microscale objects through opaque surfaces as long as their density significantly differs from that of their surroundings.

Despite their small size, several microrobots are capable of imparting enough force to perform microsurgery operations. Solovev et al. observed that asymmetrically rolled-up nanotubes moved in a corkscrew trajectory instead of a straight line trajectory, allowing them to drill and embed themselves into biomaterials [60]. Similarly, the ultrasound droplet vaporization microbullets mentioned in the actuation methods section were capable of deeply cleaving, penetrating, and deforming cellular tissue [29]. Wang et al. showed that tubular microdrillers with sharp tips were able

to drill into porcine liver tissue *ex vivo* under an external rotating magnetic field [61]. Tetherless microgrippers remotely triggered by temperature and chemical stimuli were able to grasp and remove live cells from tissue *in vitro* [44]. The grippers consisted of a bimetallic thin film structure and an actuating polymer layer that expanded under the desired environmental conditions. Another thermally activated microgripper design was able to perform an *in vivo* biopsy of a porcine bile duct. Malachowski et al. demonstrated an untethered microgripper design capable of capturing live fibroblast cells and individual red blood cells [62]. Functionalized colloidal microwheels took advantage of corkscrew motion to mechanically penetrate into fibrin gels and platelet-rich thrombi, increasing rates of blood clot fibrinolysis fivefold compared to conventional methods [63].

In addition to drug delivery, imaging, and microsurgery applications, microrobots also have the ability to detect and remove harmful substances. Guix et al. modified swarms of gold microtubes with an outer coating of alkanethiols to efficiently and quickly adsorb oil from oil-contaminated water supplies [64]. The technology is capable of isolating hydrophobic targets, such as drugs. Gold nanowires cloaked with red blood cell membranes were propelled acoustically and were demonstrated by Wu et al. to be effective toxin sponges [65]. The continuous motion of the micromotors resulted in accelerated neutralization of cell membrane-damaging toxins. Similarly, nanomotors cloaked with platelet plasma membranes avoided detrimental biofouling effects and were able to adhere to toxins and pathogens such as Shiga toxin and *Staphylococcus aureus* bacteria [66]. The addition of lectin bioreceptors to microtube engines allows the selective capture and transport of harmful *E. coli* bacteria [67, 68]. Combining magnetite nanoparticles with hydrothermally-treated fungi spores resulted in magnetically-driven biohybrid adsorbents that can remove heavy metal ions in water, capable of rapidly reducing lead concentrations from 5 ppm to 0.9 ppm [69]. This phenomenon of motion-accelerated binding and absorption was used again by Sânchez et al. to detect the presence of mercury, where fluorescent quantum dots on tubular micromotors were quenched after the binding of trace amounts of

mercury ions [70]. Liu et al. also developed a spindle-like micromotor that releases surfactant under different pH conditions, offering a potential way to detect gastric acid reflux [71].

2.4 Motivation

While an expansive variety of microrobot actuation methods and applications have been demonstrated, many improvements and further developments must still be made before practical clinical usage becomes viable. Locations such as the lungs, stomach, and colon, for example, will require microrobots that can negotiate both wet and dry conditions with complex terrains. Though extensive work has been done on chemically-powered microrobots, biohybrid microrobots, and microswimmers, the existing designs are still not optimal for use in dry environments at the microscale. Additionally, the precious metals commonly used for fabricating microtubes, nanowires, and Janus particles, such as gold and platinum, can be prohibitively expensive for mass production, despite their excellent biocompatibility and binding properties.

This project explores a tumbling microrobotic platform for all-terrain travel and biomedical applications, with a focus on targeted drug delivery. The fabrication method takes advantage of NdFeB particles and standard photolithography processes to allow for configurable magnetic alignment, arbitrary 2D geometry, and relatively cost-effective materials in the microrobot's design. Several variants of microtumbling robots (μTUM's) are designed, fabricated, modeled, and tested to quantify their mobility and viability for biomedical applications.

3. TUMBLING MICROROBOT DESIGN
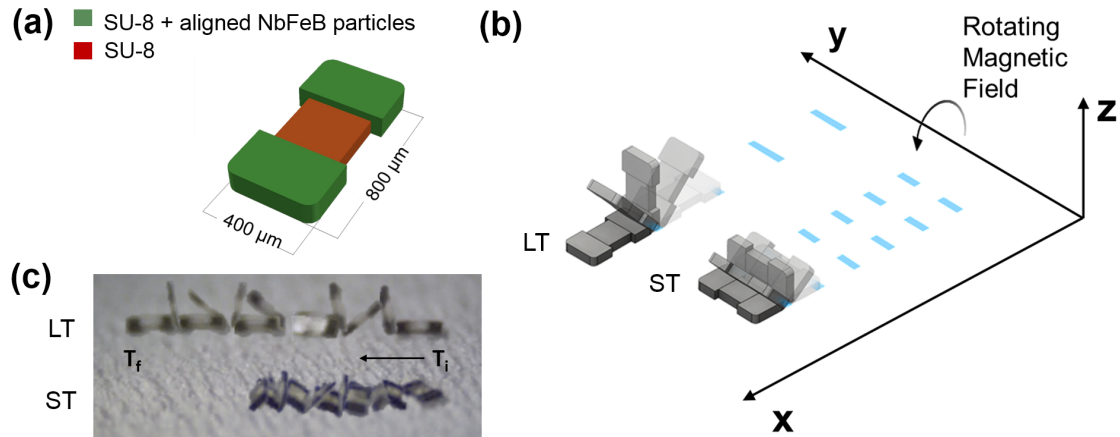
Figure 3.1. Design of the μTUM magnetic tumbling microrobot. (a) Schematic of the initial μTUM robot design. The rectangular-shaped microrobot has embedded magnetic particles at each end. (b) Depending on the alignment of the magnetic particles, a rotating magnetic field will cause the μTUM to either lengthwise tumble (LT) or sideways tumble (ST). (c) Combined video stills demonstrating both types of tumbling locomotion [72].

The μTUM robot is a rectangular SU-8 photoresist block with a high concentration of neodymium particles embedded within the photoresist polymer (Fig. 3.1(a)). The outer surface can be functionalized with a drug payload for targeted drug delivery purposes or coated with polydimethylsiloxane (PDMS) for better surface traction. Due to the high magnetic remanence of neodymium, the robot shows a stronger magnetic response than similar nickel and iron oxide-based robots. Additionally, the hard magnet properties of neodymium allow the robot to permanently retain any particular direction of magnetic polarity, regardless of its geometry. This configurable magnetic alignment allows separate μTUM robots to tumble in different modes while maintaining identical dimensions and geometry (Fig. 3.1(b)). Using the standard photolithography processes, the robot can be fabricated into any 2D geometry, whether

as a monolithic block or a block composed of multiple photoresist pieces. Under a external rotating magnetic field, the μTUM robot tumbles end over end to propel itself forward (Fig. 3.1(c)).

3.1   Design Overview
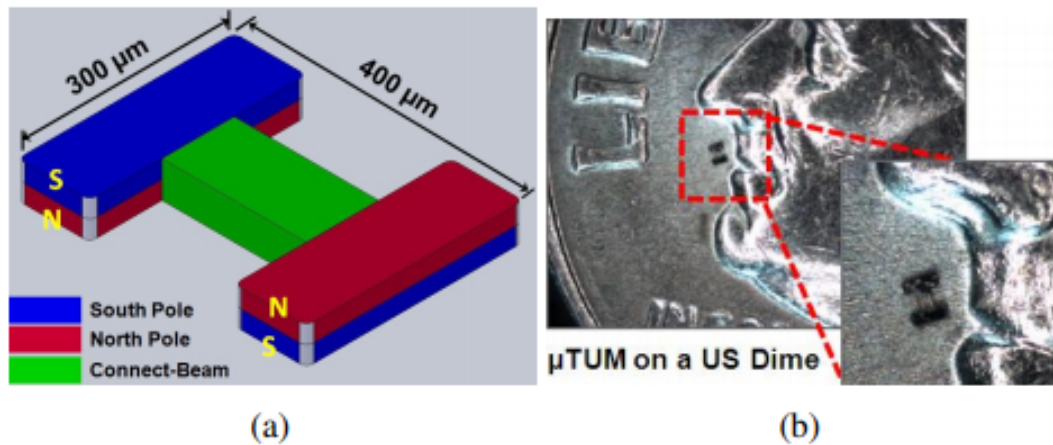
Figure 3.2.   Jing et al. design of the μTUM magnetic tumbling microrobot. (a) Schematic of μTUM robot. (b) μTUM robot on a US dime [73].

In a previous study, Jing et al. introduced a dumbbell-shaped tumbling microrobot using a similar fabrication method and NdFeB particles for magnetization (Fig. 3.2) [73, 74]. The robot is actuated by an external, uniform magnetic field that alternates between vertical and horizontal alignment, using continuous forward momentum to propel the robot through one complete rotation (Fig. 3.3). Good timing control of the alternating field is critical for maintaining the motion cycle. If the robot does not reach particular orientation angles at stages in the cycle, it risks sliding and falling backwards. By moving using tumbling motion instead of sliding motion, the robot maintains constant contact with the surface of the ground while minimizing contact area. Sliding or dragging a microscale object across a surface greatly increases stiction

forces and the forces required to move the object. Additionally, unlike the stick-slip or impact-driven motion mentioned in Chapter 2, tumbling motion is found to be well-posed for tackling rough surfaces and complex terrains.

The robot design discussed in this work is an extension of the aforementioned research with several improvements and additional characterization of the mobility and potential applications. The fabrication process and material composition of μTUM robot remains largely the same as before. The actuation method and magnetization process, however, has been simplified greatly. By replacing the alternating magnetic field with a rotating magnetic field, the precise field timing and robot reliance on forward momentum becomes unnecessary. While the old design required two rounds
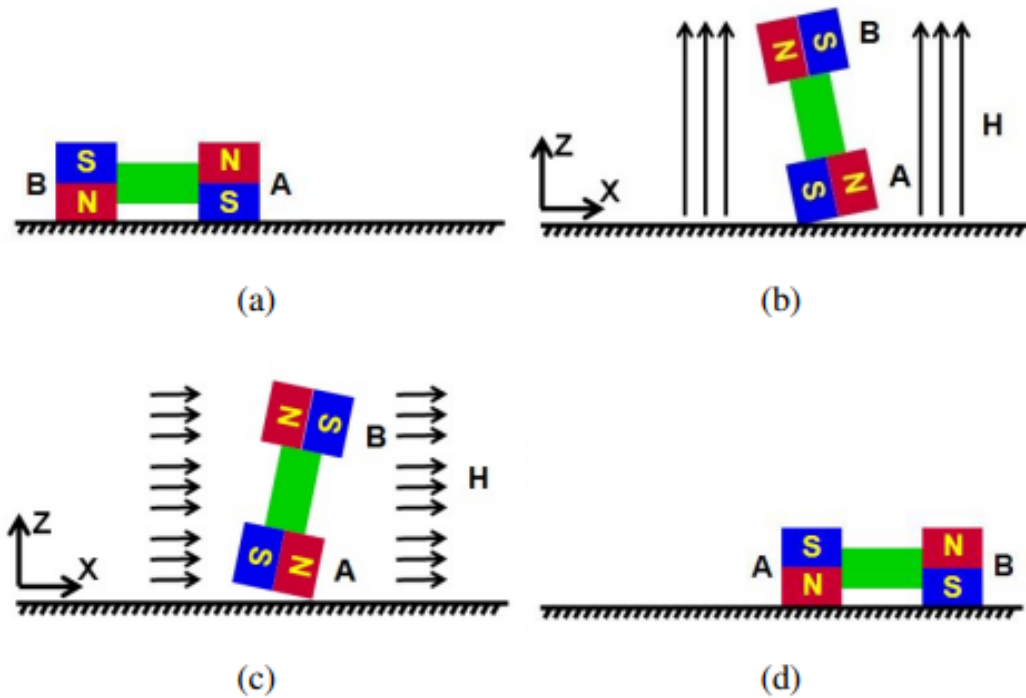
Figure 3.3. Motion mechanism of Jing et al.'s μTUM robot. (a) Initial position. (b) Vertical magnetic field applied to erect the robot. (c) Horizontal magnetic field applied to finish the tumbling motion. (d) Final position of robot after one tumble cycle [73].

of curing and magnetization to achieve the desired magnetic polarization, using a rotating magnetic field instead reduces this requirement to just one round of magnetization. The minimum requirement for the rotating field to work is a single, uniform magnetic polarization along the entire magnetic volume of robot.

The largest dimension of the robot was extended from 400 μm to 800 μm. This size is still in the microscale, but allows the orientation of the robot to be more easily seen to the naked eye. Additionally, it is a comfortable size for manually manipulating the robot's position/orientation and transporting it between different workspaces, which is helpful for experimental setup and may be helpful in clinical applications.

Neodymium is still preferred due to its high magnetic remanence and hard magnetic properties. Magnetic remanence is the amount of magnetization left in a ferromagnetic material after an external magnetic field is removed. Neodymium has a very high magnetic remanence of 1-1.3 T due to its high saturation magnetization and its nature to strongly resist demagnetization [75]. Compared to ferrite, another commonly used magnetic material with a remanence of 0.35 T [76], neodymium will be subject to higher actuating forces and torques once exposed to an external magnetic field again. Because neodymium is a hard magnetic material, the orientation of its magnetic polarity is also retained permanently. This is in contrast to soft magnetic materials such as nickel and iron-silicon alloys. These materials are only temporarily magnetic, only becoming magnetized after an external magnetic field is applied. The direction of their temporary magnetic polarity is reliant on their physical geometry/arrangement, which can limit design possibilities. Additionally, soft magnetic materials tend to exhibit weaker magnetic responses than hard magnetic materials as well. While advantageous for mobility, neodymium is not without drawbacks either. Neodymium, along with nickel, is known to be far less biocompatible than iron-oxide materials. It is also a difficult material to fabricate and machine at the micro-/nanoscale, which can discourage more complex designs. This body of research, however, tries to work around these limitations by combining neodymium particles with standard photolithography processes.

Cylindrical or spherical geometry will result in a more predictable, precise rolling motion compared rectangular geometry, but it is difficult to fabricate neodymium microrobots with this geometry. Neodymium particles, though mildly spherical, typically come in varied sizes with uneven shapes. Photolithography techniques are limited to 2D extrusions and cannot form curved three dimensional geometry. It is possible to fabricate cylinders from photoresist, but the aspect ratio would be less than ideal due to layer height restrictions. These restrictions stem from the penetration depth of the light used degrade/strengthen the photoresist. Any cylinders larger than 200 μm in diameter would resemble thin wafers more than wheels or rolling logs, and are very prone to tipping sideways. Additionally, the length of the rectangular μTUM robot would be longer than the diameter of a cylindrical robot with the same magnetic volume. With one full rotation of the external magnetic field, the former would travel much farther forward than the latter. It can also be argued that the μTUM robot's large contact area (during half of the tumbling cycle) help stop it from slipping down steep inclines. This is in contrast to a cylinder or a sphere, which maintains line or point contact respectively, for the entire duration of motion. For these reasons, a tumbling, rectangular design was chosen over a rolling, circular robot.

3.2   Magnetization Configurations

When the alignment of the external field's magnetic polarity differs from that of the μTUM robot, a magnetic torque is induced on the robot until it is realigned with the field. Applying a continuously rotating magnetic field along a rotational axis parallel to the horizontal plane causes the robot to rotate about the same axis. If this rotating field is applied on a robot that is resting on a surface, the result is a forward tumbling motion, where the robot propels itself by continuously flipping end over end. Fig. 3.1(b) depicts the resulting motion of the microrobot over a flat surface with no-slip conditions.

Alignment Axis	x-axis	y-axis	z-axis
Isometric View			
Top View			
Side View			

- North Pole
- South Pole
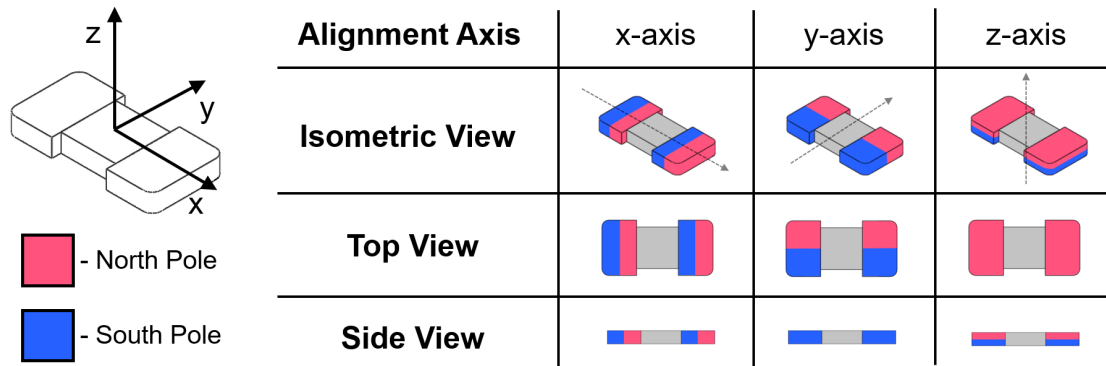
Figure 3.4. Visualization of internal magnetic alignment along the robot's three major axes [72].

Two distinct tumbling motions, a lengthwise tumbling motion and a sideways tumbling motion, can be set for the μTUM robot. These modes depend on the direction of magnetic polarity that was set during the magnetization process. The embedded neodymium particles can be uniformly aligned along any direction, so long as the fabrication method permits it. When the poles are aligned along one of the robot's major geometric axes, as defined in Fig. 3.4, μTUM will either tumble about its length or tumble about its width. Under the same external rotating field, a lengthwise tumbling μTUM robot will travel faster than a sideways tumbling μTUM robot. The lengthwise design, however, also requires more force to raise up from a flat initial resting position, due to its longer lever arm. Since speed was deemed to be more important for locomotive purposes, the lengthwise tumbling design was chosen to be the primary configuration of the μTUM robot. To determine the correct magnetic alignment for enabling this type of tumbling motion, the equilibrium states of several μTUM alignment configurations were analyzed.

The robot's initial position is defined in Fig. 3.5 and all forces apart from magnetic torque are ignored in this static analysis. It can be observed that there is only one configuration where the robot consistently moves to the upwards lengthwise position necessary for lengthwise tumbling. This case occurs when the robot is magnetically aligned along its x-axis and is influenced by a vertical horizontal field. There is
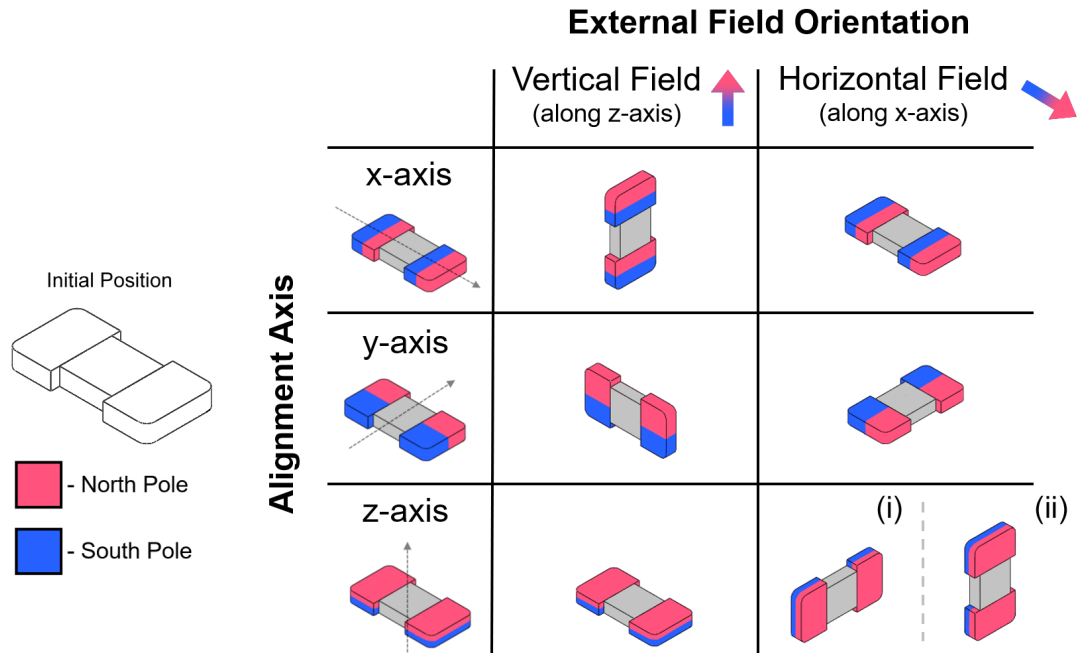
Figure 3.5. Equilibrium resting states of each major axis alignment configuration under horizontal and vertical external magnetic fields. Note: for z-axis alignment, both (i) and (ii) are possible under the same conditions, but (i) is in a lower energy state than (ii) and thus more likely to occur in practice [72].

another configuration in which the upwards lengthwise position is seen (Fig. 3.5(ii)), but in this case, an upward sideways position (Fig. 3.5(i)) is also possible under the same field orientation. Because the sideways position is at a lower energy state than the lengthwise position (due to the sideways position's lower center of mass), this other configuration tends to result in sideways tumbling. Pure lengthwise tumbling is only guaranteed in the former case, where the robot is magnetically aligned along its geometric x-axis. As a result, the robots used for majority of the experiments are magnetically aligned in this manner and are optimized for lengthwise tumbling.

3.3   Microrobot Fabrication

3.3.1   Material Composition

The initial iteration of the μTUM robot in this body of research consists of a polymeric-based microstructure with (i) two sections containing embedded neodymium-iron-boron (NbFeB) particles at the ends and (ii) one non-magnetic bridge part connecting them (Fig. 3.6). The photoresist used SU-8 50 (Microchem Inc., USA), which cures into a rigid solid once exposed to UV light. This initial design was used for mobility characterization tests that measured the performance of tumbling locomotion over various surfaces, and contained SU-8 doped with NbFeB particles (Magnequench MQFP 5μm, USA) at a concentration of 10 g/50 mL. Later design iterations, used for simulation verification and biomedical applications, consist only of SU-8 50 with embedded magnetic particles. These robots had a higher concentration of particles (30 g/50 mL) to improve magnetic response. The higher concentration of particles increased the mass ratio between the NdFeB particles and raw SU-8 resin to 1:3.
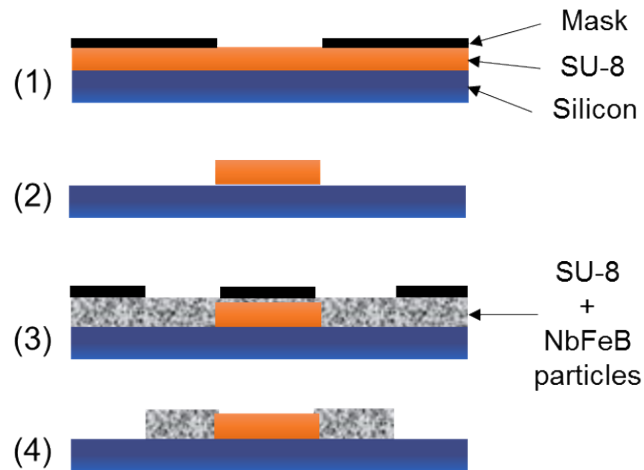
Figure 3.6.   Photolithography process followed for the fabrication of the initial three-segment μTUM robot [72].

3.3.2 Photolithography Steps

The three-part μTUM robot is made from a two-step photolithography process, where the non-magnetic middle section is first photo-patterned from bare SU-8 50 (Fig. 3.6(a), steps (1) and (2)), and then the robot ends are fabricated from SU-8 doped with NbFeB particles (Fig. 3.6(a), steps (3) and (4)). To pattern the middle polymeric section, the standard recommended protocol for structures of 100 μm thickness was followed. The SU-8 50 is spin-coated at 1000 rpm on a silicon wafer for 30 seconds and then undergoes a soft baking process consisting of two consecutive steps of 10 minutes at 65°C and 30 minutes at 95°C in order to evaporate the solvent. The full wafer is then exposed in a mask aligner (UV (350-400nm), Suss MA 6 Mask Aligner, SUSS MicroTec) by using a mask with a design corresponding to the middle section of the robot. A post-exposure bake (1 minute at 65°C and 10 minutes at 95°C) is performed before the removal of the non-polymerized SU-8 with SU-8 developer (Microchem Inc., USA). It should be noted that while standard SU-8 is formed in layers of approximately 100 μm, there are variants of SU-8 that can be formed in layers in excess of 400 μm. These variants can be potentially incorporated into future μTUM designs for greater dimensional variation.

For the monolithic μTUM robots used in the simulation verification and biomedical application experiments, the midsection of robot is magnetized as well, meaning that the two-step photolithography process can be simplified to just a single-step process for these robots. This simplified process can be seen in Fig. 3.7, steps (1) and (2).

3.3.3 Magnetization Process

Though NdFeB particles can be magnetized individually ahead of time, the particles will settle in a disorderly fashion when collected in bulk. The randomly oriented fields from each particle can negate the effects of adjacent particles, reducing the overall magnetic strength of the collective particles. Exposing these particles to a strong
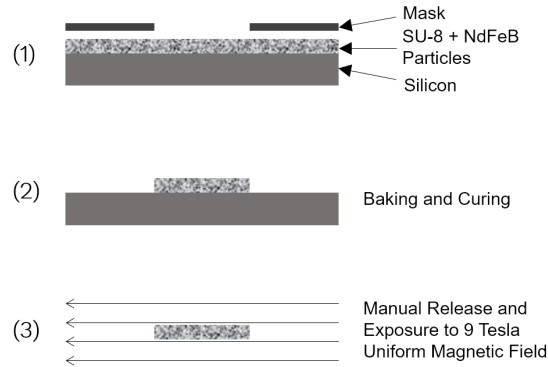
Figure 3.7. Photolithography and magnetization process for the fabrication of the improved microscale magnetic robot [77].

external magnetic field is necessary to align all of them in a uniform direction and greatly enhance the magnetic responsiveness of the resulting μTUM robot. In this project, two sources of magnetization fields were used. The first source was a pair of large permanent magnets that were placed close to the photoresist wafer during the fabrication process. Later on, the process was improved with equipment that could project high-strength, uniform magnetic fields over a small workspace. This improved process still works after the robots are fabricated and the magnetic particles are already hardened in place, providing more flexibility to the fabrication/magnetization process.

Magnetization Using Nearby Large Magnet

For the μTUM robots with three distinct segments, which include Jing et al.'s predecessor design and the robots used for mobility characterization tests, two permanent magnetic discs (3 inches dia. x 1/8 inch thick NdFeB, Grade N42, K & J Magnetics Inc.) were used for the magnetization process. These magnets were either placed vertically over the wafer or directly to the side of the wafer while the photoresist soft-cured over a hot plate (Fig. 3.8). A vertical position resulted in magnetic alignment for sideways tumbling and a horizontal position resulted in magnetic align-

ment for lengthwise tumbling. The magnetic fields projected from the permanent magnets were neither very strong nor uniform over the area of the wafer, resulting in robots that had varying magnetic alignments and weak magnetic responses. Only a few of the robots, usually the ones closer to where the magnets were centered, emerged from the process with the correct lengthwise or sideways alignment. Many others emerged with magnetic alignments that were at slight angles from the major geometric axes, altering their motion characteristics.
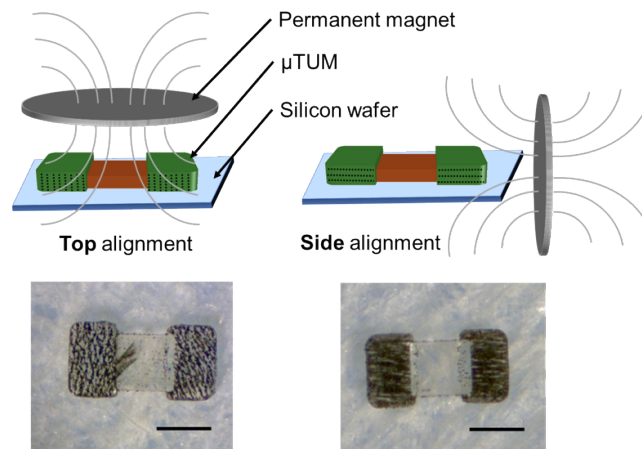
Figure 3.8.   Magnetic particle alignment techniques using nearby large magnets. Magnets located above the robot result in alignment along the geometric z-axis and sideways tumbling (ST); magnets located beside the robot result in alignment along the geometric x-axis and lengthwise tumbling (LT). Note that the field projected from the magnets is not uniform. Scale bar, 300 μm [72].

Magnetization Using Uniform, High-Strength Magnetic Field

NdFeB particles will magnetically realign themselves, even after the surrounding photoresist has cured and hardened them in place, if subjected to a magnetic field greater than a threshold strength of about 1 T. This behavior was exploited in later μTUM robot designs, where an improved magnetization process was used to make the robots. The new process was made possible with a PPMS Dynacool machine (Quantum Design), which is capable of applying uniform magnetic fields of up to 9 T

within a small, centimeter-scale workspace. The machine is also capable of measuring the remanent magnetization of loaded samples. After photolithography and curing into rigid bodies, the μTUM robots were loaded into the PPMS machine on a quartz sample holder and secured with several rolled layers of Kapton tape (Dupont), after which they were exposed briefly to a 5 T magnetic field. The resultant μTUM robots exhibited more consistent magnet alignment with better yield rates and a significantly stronger magnetic response. This improved response means higher magnetic torques are exerted on the microrobot under the same magnetic field. While older robots required minimum external field strengths of around 7 mT in dry environments to start tumbling, many improved μTUM robots were observed to tumble at field strengths of 3 mT or less. Though higher torque will not significantly affect speed in low-drag environments or slipping under various conditions, it can be beneficial for movement in situations with high stiction and/or viscous drag forces.

3.4 Geometric Variations

As stated in the previous section, the initial design iteration of the μTUM robot resembles the rectangular dumbbell-shaped robots presented in Jing et al.'s work [74]: two separate NdFeB-doped ends with a clear photoresist midsection. While this latter section remained nonfunctional during the mobility characterization tests, it can be functionalized in future studies with a dissolvable payload responsive to changes in the surrounding chemistry, light, acidity, and temperature. Keeping this nonfunctional section in the initial design more accurately reflected the robot's ability to move when burdened by a large payload (that could have been replaced by additional magnetic volume).

After this initial three-part rectangular design, several geometric variations were also introduced. These variations include robots with different geometry on the ends of the 'dumbbells', robots with spikes for better traction, and robots with large pores for better drug retention.

3.4.1 Mobility Characterization
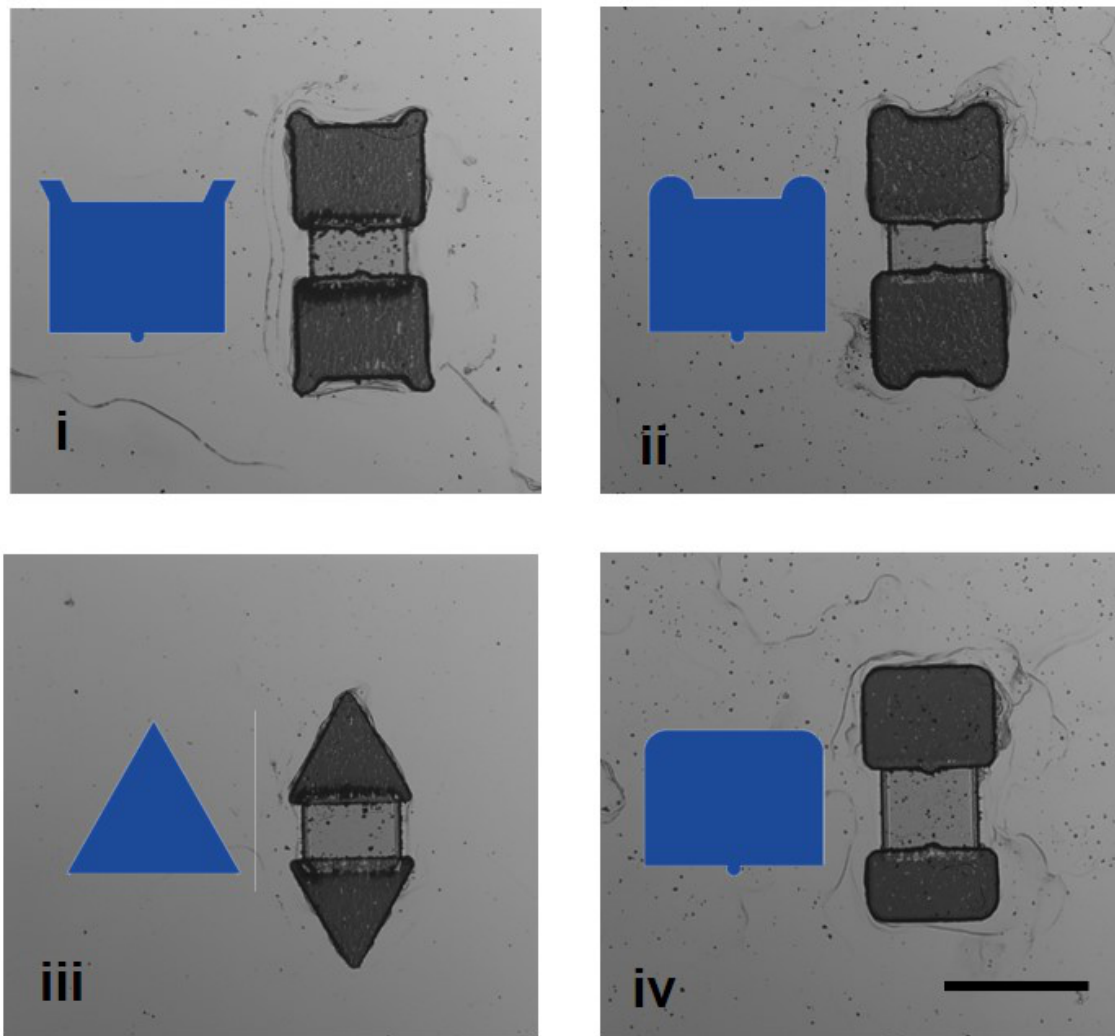
Figure 3.9. Optical images of the different geometric variations on the μTUM ending sections that have been explored: (i) sharp corners, (ii) rounded corners, (iii) triangles, (iv) (asymmetric) rounded rectangles. Scale bar, 300 μm [72].

The geometry on the magnetized ends of the μTUM robot was varied to explore its effect on the robot's locomotion. The number of corners, the sharpness of the corners, and the protrusion of the corners were varied to see if these factors would significant affect the robot's performance. The effect of symmetry was also explored by fabricating robots with ends of slightly different lengths. It was questioned whether

the sharpness of the corners would help the robot gain traction or hamper it by getting caught on rough surfaces. Would the robot still be able to balance and tumble on one corner instead of two? Would the unbalanced center of mass in the asymmetric design result in faster tumbling?

For testing purposes, the basic rectangular geometry was chosen as the control design ('rounded rectangles'), due to its uniform flat edges and predictable behavior, and the other designs were compared against it. For all the geometric variations considered in the mobility characterization tests, the midsection of the robot remained unmagnetized. Four types of geometries were considered in total: (i) rounded corners, (ii) sharp corners, (iii) triangles, and (iv) rounded rectangles (Fig. 3.9). For the rectangles geometry, two different cases were considered: a symmetric version (Fig. 3.1(a)) and an asymmetric version (Fig. 3.9(c)(iv)).

3.4.2 Simulation Design Optimization

Several additional geometric variations (Fig. 3.10) were virtually analyzed in the simulation model discussed in Chapter 4, but not experimentally tested. These variations only contain changes to the side profile of the robot to allow for two-dimensional simulation, which runs faster than fully three-dimensional simulation. The goal for these variations was to use the simulation results to determine an optimal design based on the maximum velocity the robot achieved and the maximum incline angle it could climb. None of these variations contain an unmagnetized midsection and are assumed to be uniformly magnetized along the entire robot's length. This adjustment was made to reduce the complexity of the simulation model and reduce the time needed to run it. Because all geometry must be hard-coded into the simulation model as simple polygons, the designs for the simulation variations avoided incorporating features with complex curvature or complicated design elements. This limitation influenced what designs were ultimately tested and led to four variations: a control, 'cuboid' rectangular shape, a shape with spikes in the middle, a shape with spikes on
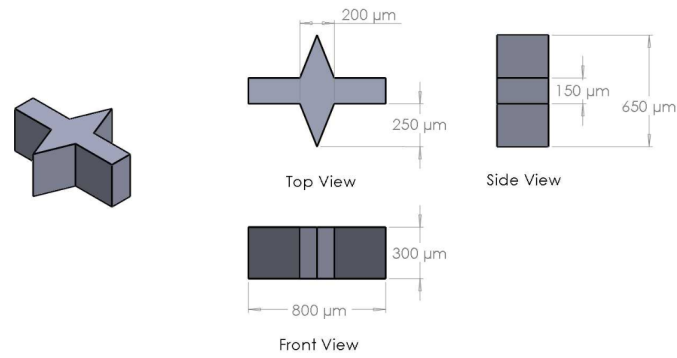
(a) Design for spiked shape μTUM robot.
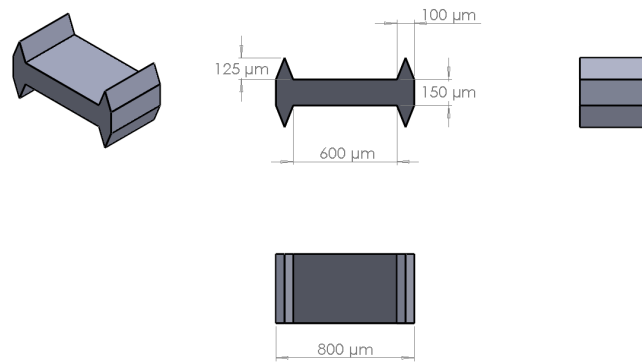
(b) Design μTUM robot with spiked ends.
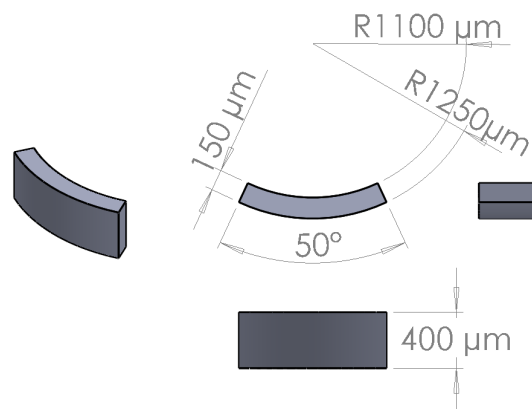
(c) Design for curved shape μTUM robot.

Figure 3.10. Geometric variations of simulation μTUM robot for design optimization [78].

the end, and a circular curved shape. It was proposed that spikes might help reduce slipping on inclines and that the unique form of the curved shape might result in unexpected benefits for the tumbling motion.

3.4.3   Biomedical Applications Testing

For testing payload diffusion, discussed in further detail in Chapter 6, the un-magnetized midsection was not further utilized to contain a functional drug payload. The poly(lactic-co-glycolic acid) (PLGA) solution used for the experiments could not be solidified and incorporated inside the robot. Instead, the midsection was replaced with more of the magnetized NdFeB-photoresist mixture and two circular cut-outs 200 μm in diameter were made on the robot to create more surface area (Fig. 3.11). Since the PLGA solution was coated on the exterior surface of the robot, adding more surface area would allow more of the coating to adhere on. Furthermore, it was hoped that surface tension would keep additional PLGA trapped within the inside of the cut-outs, maximizing payload volume.
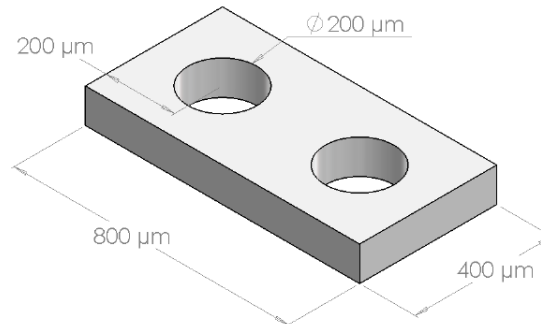
Figure 3.11. Design variation and dimensions for biomedical applications testing [77].

4. TUMBLING ROBOT MODELING

Without simulation tools, deciding design parameters for the tumbling robots is largely a trial and error process involving costly and time-consuming microscale fabrication processes. The static and dynamic behavior of the tumbling microrobot were modeled to gain insight into the limitations of the design and predict the effects of changing the robot's dimensions, geometry, and magnetization. Stiction effects are considered since they are relatively large in magnitude at the microscale compared to the effects of gravity and inertia. The tumbling motion of the μTUM robot also introduces the issue of modeling intermittent and non-point contact, which poses problems for conventional dynamic simulators. New techniques are necessary to deal with this unique behavior.

For the models discussed in this chapter, it is assumed that the robot is rigid and that its material and magnetic properties are homogeneous throughout its body. Additionally, it is assumed that surface properties at the microscale are uniform as well. While this is not true in practice, it is very difficult to model the nonlinear and often random variations that actually occur, and averaged values for surface properties are used instead. All the models also assume that the robot only moves over substrates in dry environments and that viscous drag is neglected. This limitation is because the dynamic turbulent flow generated by the rotating μTUM in fluid environments is very difficult to model and quantify, with no examples using the same geometry existing in literature. Finally, it is assumed that the external magnetic field remains homogeneous within the workspace and is uniformly aligned. Please note that portions of this chapter were previously published by Micromachines [72] and for the ASME International Design Engineering Technical Conference (IDETC) [78].
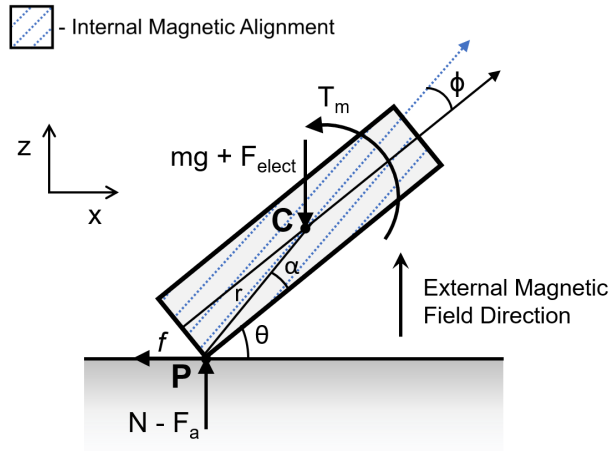
Figure 4.1. Schematic for two-dimensional μTUM model with applied forces and torques on microrobot. Point C is the center of mass and point P is the contact point. Note that adhesion force will act on the center of mass if the robot is resting flat on the ground [72].

4.1 Magnetic Torque Under External Field

Due to differences in orientation between the microrobot's magnetic polarization and that of the external magnetic field, seen in Fig. 4.1, a magnetic torque is exerted on the robot:

$$\vec{T}_m = V_m \vec{M} \times \vec{B} \tag{4.1}$$

Eq. 4.1 describes the general working principle of this torque, where V_m is the magnetic volume of the robot, $\vec{M}$ is the magnetization of the robot, and $\vec{B}$ is the external magnetic field strength. Under a static magnetic field, the torque coerces the μTUM robot to align itself with the direction of the field. Under a time-varying rotating magnetic field, the torque causes the μTUM robot to rotate forward into a tumbling motion.

4.2   Static Analysis

One of the first considerations for the μTUM robot is whether the driving external magnetic field is strong enough to rotate it up from an initial resting position, where forces due to gravity, electrostatic attraction, and surface adhesion must be overcome. A static analysis of the forces on the robot was first conducted to determine the minimum external field strengths required for upwards rotational movement. For modeling purposes, the various constituents of microscale surface adhesion, such as intermolecular bonding, Van der Waals interactions, and capillary forces, are lumped together into a single adhesive force F_a. The robot in the model is kept as basic as possible, with geometry approximated as a rectangular prism and a uniform magnetic alignment optimized for lengthwise tumbling.

Though additional forces may act on the robot due to magnetic field gradients, these forces are neglected in the model because no field gradients were intentionally applied during the experimentation process. From Eq. 4.1 in the previous section, it can be observed that the maximum magnetic torque will occur when the robot and the external field alignments are perpendicular to each other. If the robot is initially resting flat against flat horizontal surface, the external field should be vertically aligned to exert the maximum magnitude of magnetic torque on the robot. Additional applied torque from gravitational, electrostatic, and adhesive forces will resist this applied magnetic torque can prevent the robot from rotating upwards into a tumbling motion. When the external field is time-invariant, all the applied torques balance out over time and the robot comes to rest at a steady state equilibrium angle. One end of the robot will maintain contact with the surface while the other end is lifted from the substrate. Under static conditions, the end of the robot that is in contact with the substrate can be considered as a no-slip point P that is pinned to the surface. Assuming that the robot has uniformly distributed mass, the center of mass C should also coincide with the geometric center. The resultant side view free-body diagram can be seen in Fig. 4.1.

Due to the alignment errors in the magnetization method used for the initial μTUM robot design iterations, the magnetic alignment of these robots often do not coincide with any of their major geometric axes. An alignment offset angle ϕ, defined as the angular difference between the robot's actual alignment direction and the desired alignment direction, is introduced in the model to account for this discrepancy. Due to varying alignment offset angles, it is possible for these initial μTUM robots to stabilize at different steady state orientations, despite having identical geometries, applied fields, material properties, and environmental conditions. If the magnetic alignment error is too large ($>35°$), the resultant robot fails to exhibit the desired lengthwise tumbling motion and has difficulty tumbling in a controlled manner.

To determine the input torque necessary to overcome static resistive forces, inertia, and gravity, the moment equilibrium about the pinned contact point P in Fig. 4.1(a) can be analyzed:

$$\Sigma M_P = 0 = T_m - (mg + F_{elect})r\cos(\theta + \alpha) \tag{4.2}$$

$$V_m|M||B|cos(\theta + \phi) = (mg + F_{elect})r\cos(\theta + \alpha) \tag{4.3}$$

$$|B| = \frac{(mg + F_{elect})r\cos(\theta + \alpha)}{V_m|M|\cos(\theta + \phi)} \tag{4.4}$$

$$|B_{min}| = \frac{(mg + F_{elect} + F_a)r\cos\alpha}{V_m|M|\cos\phi} \tag{4.5}$$

where r is the diagonal distance between the no-slip point P and the center of mass C, θ is the orientation angle of the robot, ϕ is the magnetic alignment offset angle, and α is the angle between the corner of the robot and its center of mass (determined from geometry). F_a and F_{elect} are the adhesive and electrostatic forces respectively between the robot and the substrate. If treated as a point force, it is important to note that adhesion force F_a will act on the center of mass C if the robot is resting flat

on the substrate and will act on the no-slip point P if the robot is rotated upwards. In actuality, this adhesion force is a distributed force that is proportional to the surface area in contact with the substrate. The electrostatic force F_{elect} is another distributed force that is simplified as a point force in this model. Due to static electricity present on the surface of dry insulators such plastic, paper, and rubber, the entire robot's nonconductive body is pulled towards the substrate through an attractive electrostatic force. In practice, this force is difficult to quantify and should be reduced as much as possible to minimize unpredictable motion. Two ways of reducing charge imbalance are using a conductive metallic substrate or testing within a wet environment that can dissipate charges.

Eq. 4.4 is valid when the robot is raised and its orientation angle θ is greater than 0°. The equation describes the relationship between the strength of the external magnetic field and the robot's resultant steady state orientation. Eq. 4.5 is valid when the robot is flat against the substrate and its orientation angle θ is equal to 0°. This is the equation that approximates the minimum field strength necessary for making tumbling motion possible on a horizontal substrate, and can be used as a simple check to see if a particular design choice is viable or not. The main difference between the two aforementioned equations is that the latter equation contains an adhesion force term while the former equation does not, due to the adhesion force assumption described earlier in this section.

To estimate the unknown electrostatic and adhesion forces in Eq.'s 4.2-4.5, the inclination at which the μTUM robot begins to slip on the relevant substrate can be observed. The robot is first laid flat on the horizontal substrate and the substrate is then tilted until the robot begins sliding. At this inclination angle, the force exerted by the robot's weight down the incline matches that of static friction, and the sum of the electrostatic and adhesive forces can be written as:

$$F_a + F_{elect} = \frac{mg \sin \gamma}{\mu_s} - mg \cos \gamma \tag{4.6}$$

where angle γ is the surface inclination angle that the robot is observed to slip at.

To reduce the number of unknowns in Eq. 4.6, assumptions can be made about electrostatic and adhesive forces. In dry environments, electrostatic forces are significant on nonconductive materials because there is no aqueous fluid to dissipate individual charges. The opposite is true for wet environments or metallic substrates, where electrostatic charges are dissipated. On rough surfaces, adhesive forces are reduced because of decreased contact area between the robot and the substrate. The opposite is true for smooth surfaces, where adhesive forces are significant due to large contact areas. Therefore, the left side of Eq. 4.6 can be approximated to just the electrostatic force F_{elect} for rough, nonconductive substrates, and to just the adhesive force F_a in smooth, conductive substrates.

To determine the unknown alignment offset angle ϕ in Eq. 4.4-4.5, a strong permanent magnet can be placed directly below the μTUM robot and rotated in such a way that the external magnetic field around the robot is aligned vertically. A thin sheet of plastic should be kept between the robot and the magnet to prevent the robot from getting stuck to the magnet. The observed angular difference between the orientation that the robot settles at and the vertical direction perpendicular from the sheet should be approximately equal to the alignment error. For all robots fabricated using the improved magnetization technique, it is safe to assume that the alignment offset angle is always 0°.

Once all the unknown parameters have been determined, the static force equations described in this section can be used for estimating the minimum magnetic field strengths needed to rotate the μTUM robot from rest.

4.3   Dynamic Simulation with Intermittent Contact

Controlled tumbling locomotion is unorthodox and rarely, if ever, seen in macroscale applications. External energy fields are too weak or inefficient to rotate entire mobile robots or transportation vehicles at that scale. As a result, the dynamic behavior and modeling of this motion has not been well-studied in literature. It

would be advantageous, however, to be able to perform simulations of the μTUM robots before physically fabricating design variations.

Since the magnetic field source may not always be nearby, it is beneficial to optimize the robot's design for achieving the most mobility under limited magnetic field strengths. It is also beneficial to optimize the design for movement over as many different surfaces as possible. A flexible simulation tool for virtual design iteration and optimization would be particularly useful towards these goals. In this section, the development of such a simulation tool is discussed and the modeling techniques used are summarized. After verifying the simulation output experimentally, the tool is used to predict the motion of μTUM robots with varying geometry and an optimal design is chosen. The simulation-enhanced design process should help reduce the fabrication workload to just a small subset of the initial design variations, lowering the cost and effort necessary for microrobot development.

4.3.1 Extension of Static Analysis Model

At first, a simulation attempt was made by extending the two-dimensional static analysis model discussed in the previous section into a dynamic model. The equations of motion and methodology discussed here are very similar to those described in the two dimensional dynamic analysis of stick-slip microrobots [79]. Using the same applied forces and notation outlined in Fig. 4.1, the following kinematic equations of motion can be formulated:

$$C_x = P_x + r\cos(\theta + \alpha)$$
$$\ddot{C}_x = \ddot{P}_x - r\ddot{\theta}\sin\theta - r\dot{\theta}^2\cos\theta$$

(4.7)

$$C_z = P_z + r\sin(\theta + \alpha)$$
$$\ddot{C}_z = \ddot{P}_z + r\ddot{\theta}\cos\theta - r\dot{\theta}^2\sin\theta$$

(4.8)

These equations describe the kinematic relationship between the center of mass of the robot and the point in contact with the substrate. Based on the applied torques and forces, the following kinetic equations of motion can be formulated as well:

$$m\ddot{C}_x = -f \tag{4.9}$$

$$m\ddot{C}_z = N - mg - F_a - F_{elect} \tag{4.10}$$

$$J\ddot{\theta} = T_m - rN\cos(\theta + \alpha) - rf\sin(\theta + \alpha) \tag{4.11}$$

where J is the moment of inertia of the μTUM robot. It is assumed that the robot is still in a dry environment and that viscous drag forces are negligible. Additionally, the electrostatic forces and adhesive forces are still treated as point loads while the alignment offset angle is assumed to be zero.

When examining Eq. (4.7-4.11), it can be observed that they make up an underdefined system, with only five unique equations of motion and seven unknown quantities: N, $\ddot{\theta}$, $\ddot{C}_x$, $\ddot{C}_z$, $\ddot{P}_x$, $\ddot{P}_z$, and f. However, when taken in a case by case basis, solving the system becomes more tractable.

In previously discussed static model, it is assumed that the point P is pinned to the substrate and cannot move. In this section's dynamic model, the robot undergoes tumbling motion and the point P can: (1) remain a pinned, no-slip point, (2) slide along the substrate, or (3) break contact with the substrate. By initially assuming the point P is pinned, the unknown values $\ddot{P}_x$ and $\ddot{P}_z$ can be set to zero and the system of equations can be solved. The solution from this assumption can result in three cases:

Case 1: If normal force N was found to be negative, then the pinned point P must have broken contact with the substrate and the robot is off the ground. Eq. (4.7,4.8,4.11) can then be solved by assuming that the normal force N and the friction f are both zero.

Case 2: Assuming the Coulomb friction model is valid, if the resulting friction force f is found to be larger than the normal force N multiplied by the friction coefficient μ (the maximum possible friction force), then the robot must be slipping on the substrate instead of tumbling without slipping. The point of contact is sliding and Eq. (4.7-4.11) can be resolved by setting friction force f to this maximum friction force and leaving the horizontal acceleration of the contact point $\ddot{P}_x$ as an unknown.

Case 3: If neither of the conditions in the preceding cases were met, then the initial assumption that the robot is not slipping and in contact with the substrate is valid and the initial solution is satisfactory.

Due to the discontinuous nature of this model and the many conditions that need to be considered, a simple time-stepping Euler method was considered the most straightforward way to integrate the equations of motion. Though more rigorous ordinary differential equation solvers could be used to reduce the amount of numerical error, these solvers are typically designed for continuous functions and would have to be reset every time a case/condition changes.

In addition to the conditions and changes that apply for the point of contact, the equations of motion must also be adjusted as the robot tumbles forward and the point of contact changes. The magnitude of the adhesive force must be varied as well, depending on how much surface area is in contact with the substrate. These two behaviors were incorporated into the simulation model by examining the orientation angle θ of robot at each time step and altering the equation signs and force magnitudes accordingly.

The parameters in Table 4.1 were used to generate the dynamic simulation model shown in Fig. 4.2. Paper was used as a test substrate material since it is used later on in mobility characterization experiments and also contains both electrostatic and adhesive forces in significant quantities.

The resulting simulation model can be used to visualize and quantify the robot's trajectory under during tumbling locomotion. It can also be used as a tool for predicting when the robot will slip and lose traction on various surfaces. This simple

Table 4.1. Parameters for μTUM robot on paper.

Description	Value	Units
μTUM Length (L)	0.8×10^{-3}	m
μTUM Width (W)	0.4×10^{-3}	m
μTUM Height (H)	0.1×10^{-3}	m
Mass (m)	1.6071×10^{-7}	kg
Electrostatic Force (F_{elect})	3.2022×10^{-6}	N
Friction Coefficient (μ)	0.3	-
Magnetic Alignment Offset (ϕ)	0	degree
Magnetic Volume (V_m)	2.9×10^{-11}	m^3
Magnetization ($|\boldsymbol{E}|$)	15000	A/m
Coefficient of adhesion force (C)	3.7148	N/m^2

dynamic model, however, still has several limitations. It is not straightforward to alter the geometry of the simulated robot apart from changing the dimensions of the rectangle and three dimensional geometry also can not be evaluated with this tool. Additionally, the collision model for this tool was quite basic. To prevent the simulated robot from going into and through the substrate surface, the simulation was
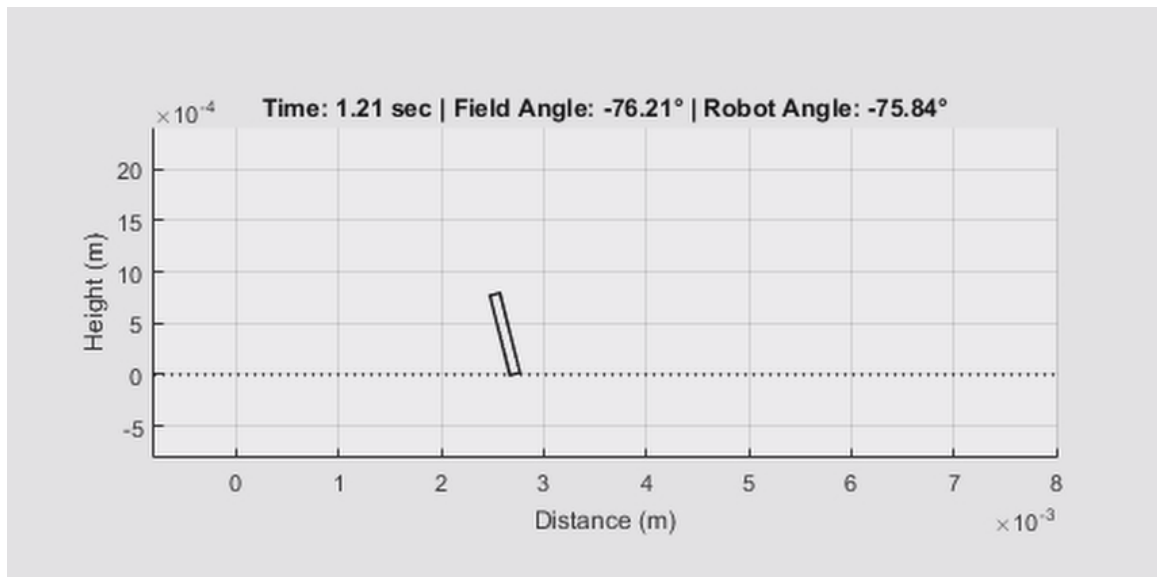
Figure 4.2. Two-dimensional dynamic simulation of μTUM robot moving under a 1 Hz, 10 mT rotating magnetic field.

programmed to simply move the robot position upwards every time interpenetration was detected. This collision model is quite simple and does not accurately reflect the true nature of the contact interaction. On substrates that are not perfectly flat, the collision model may fail to recognize some interpenetration cases since it only considers the corners of the robot.

4.3.2 Challenges and Existing Simulation Techniques

To get around the limitations of the aforementioned simulation model and develop a better holistic design tool, focus was shifted toward previous simulation methods and more advanced modeling techniques. A critical challenge for simulating the tumbling microrobot is modeling the intermittent and non-point contact between the robot and the substrate, which changes constantly throughout the tumbling motion. As the μTUM robot tumbles over a planar surface, it constantly alternates between a line contact mode and an area contact mode. This corresponds to an edge of the robot striking the substrate and a face of the robot striking the substrate. The model in the previous section and many existing dynamic simulation methods [36,79] implicitly assume that the contact between two bodies can be modeled as point contact. Contact points are chosen *a priori* in an ad hoc manner to represent the contact patch. For the μTUM robot, since the contact patch is actually time-varying, it is not possible to choose a contact point *a priori*. Thus, this assumption introduces inaccuracies in the resulting simulation. To complicate the matter, the contact point may also be in no slip or slipping states as well, as seen in the previous section.

Recently, Xie et al. developed principled methods [80–82] to simulate contacting rigid bodies with planar convex and non-convex contact patches. Similar techniques are used here for simulating the motion of microrobots where the contact between the robot and the substrate is intermittment and not restricted to purely point contact. The model in [80] is extended to handle the torque applied from a rotating magnetic field and surface area-dependent adhesive forces acting on the rigid body microrobot.

Additionally, a procedure based on contact modes is developed to compute the changing magnitude of the adhesive forces.

4.3.3   Model Methodology

The improved simulation makes use of the differential complementarity problem (DCP) model, posing the discrete-time dynamics model of the robot as a mixed nonlinear complementarity problem (MNCP).

Modeling the intermittent contact between bodies in motion as a complementarity constraint was first done by Lotstedt [83]. Subsequently, there was a substantial amount of effort in modeling and dynamic simulation with complementarity constraints [84–88]. The DCP that models the equations of motion usually can not be solved in closed form format. Therefore, a time-stepping scheme has been introduced to solve the DCP. Depending on the assumptions made when forming the discrete equation of motions, the discrete-time model can be divided into a mixed linear complementarity problem [89, 90] and a mixed non-linear complementarity problem [91, 92]. Furthermore, depending on whether the distance function between the two bodies (which is a nonlinear function of the configuration) is approximated or linearized, the time-stepping scheme can also be further divided into geometrically explicit schemes [84, 86] and geometrically implicit schemes [80, 91, 92].

All of the time-stepping schemes mentioned above assume the contact between two objects to be point contact. However, at the microscale, the influence of adhesion and friction, which both scale with surface area, become more pronounced. Recently, Xie et al. introduced a dynamic model that takes non-point contact (where the contact mode could be point contact, line contact, or surface contact) into account [80]. The model belongs to a geometrically implicit time-stepping scheme, in which the distance function depends on the geometry and configurations of the rigid body. For this simulation, the model was extended to handle the surface area-dependent adhesive forces acting on the μTUM robot.

There has been much effort to model and understand the effect of non-point frictional contact [93–95]. The so-called soft-finger contact model [96] is used in this work for the dynamic simulation. This soft-finger contact model is based on a maximum power dissipation principle and it assumes all the possible contact forces or moments should lie within an ellipsoid.

As stated in Chapter 2 and in the static modeling section, adhesion becomes significant in the microscale and can be considered as the combined effect of forces that may stem from capillary effects, electrostatic charging, covalent bonding, hydrogen bonding, Casimir forces, or Van der Waals interactions [97]. Because these forces can be unpredictable and difficult to model individually, they are lumped together into a single adhesion force. It is assumed that its effect is insignificant if there is no direct contact between the microrobot and the substrate. Thus, an empirical relationship can be made where this lumped adhesive force is proportional to the surface contact area. This relationship is useful because the dynamic model is capable of predicting the time-varying surface contact area. Electrostatic force, meanwhile, is treated as a constant, since the distance between the microrobot and the substrate undergoes minimal change as the robot moves.

The general equations of motion has three key parts: (i) Newton-Euler differential equations of motion giving state update, (ii) algebraic and complementarity constraints modeling the fact that two rigid bodies cannot penetrate each other, and (iii) a model of the contact force and moments acting on the contact patch. For general rigid body motion, the model of contact forces and moments use Coulomb's assumption that the normal force acting between two objects is independent of the nominal contact area between the two objects. This is a reasonable assumption for nominally rigid objects at macroscopic length scales, where the inertial forces are dominating. However, at the length-scale of microrobots, the force of adhesion between the contacting surfaces is comparable to inertial forces. Thus, the contact model should also consider the effect of the surface-area dependent forces. These forces, combined under a single adhesive force, are illustrated in Figure 4.3.

In [80], the concept of an equivalent contact point (ECP) to model non-point contact between objects was introduced. The ECP is defined as a unique point on the contact surface that can be used to model the surface (line) contact as point contact where the integral of the total moment (about the point) due to the distributed normal force on the contact patch is zero. In this case, the ECP defined is the same as the center of friction. Between two rigid bodies, a pair of ECP's exist as well as complementarity conditions for nonpenetration. The solution to these ECP's is given by a minimization problem and can be found to get the complete contact model between the two rigid bodies.

It can be shown that the problem formulation using the power loss over the whole contact patch can be reduced to a friction model for point contact with the ECP as the chosen point. After specifying the friction model, a law or relationship that bounds the magnitude of the friction forces and moments in terms of the magnitude of the normal force is also necessary [94]. An ellipsoidal model for bounding the magnitude of tangential friction force and friction moment is used for the simulation. This friction model has been previously proposed in literature [80, 92, 94, 98] and has some experimental justification [95].

A velocity-level formulation and an Euler time-stepping scheme is again used to discretize the system of equations of motion for the μTUM robot and simulate the dynamic behavior. The Lagrange multipliers of contact constraints are used to identify which side or boundary of the robot is in contact with the surface at the current time step and the adhesive impulse is then computed from this data. Afterwards, this impulse is fed as input for the next time step. The resulting simulation model is capable of accurately simulating various μTUM robot geometries in three dimensions over uneven terrain, adding new parameters for design optimization and addressing the limitations of the model developed in the previous section. Further detail on the simulation methodology, the equations of motion used, and conceptual proofs of the stated assertions for this improved simulation model can be found in [78].
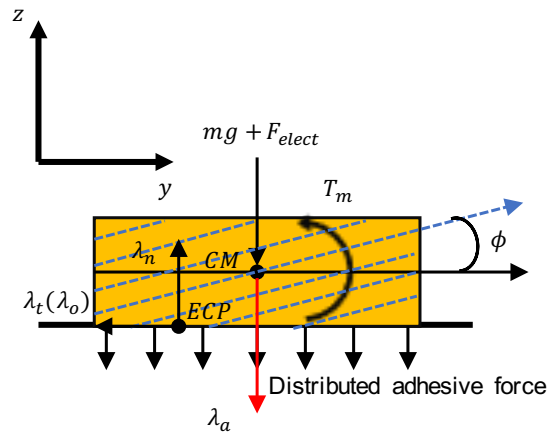
(a) Robot in surface contact with flat substrate in 2D.
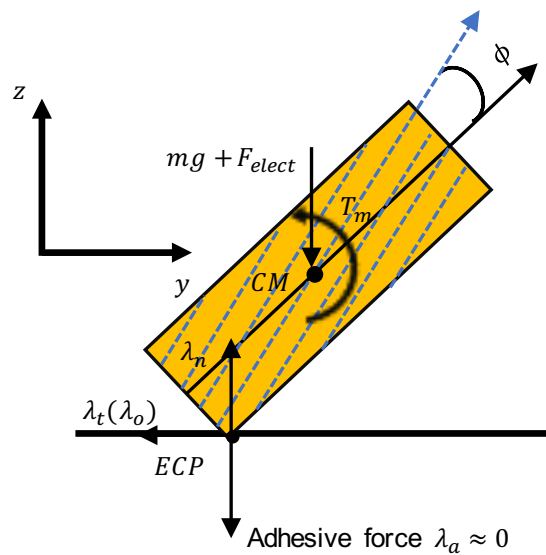
(b) Robot in line contact with flat substrate in 2D.

Figure 4.3. Schematic for improved simulation μTUM model with applied forces and torques on microrobot. CM is the center of mass and the blue dashed lines represent the internal magnetic alignment. This model more accurately models adhesive force by distributing it uniformly over the surface area. When the robot has line contact with the surface, adhesive force is almost zero [78].

5. MOBILITY CHARACTERIZATION EXPERIMENTS

The initial design of the μTUM robot (rounded rectangle geometry with alignment tuned for lengthwise tumbling) was tested on a dry paper surface (Kimwipes, Kimtech Science TM, USA) in order to evaluate its performance under varying field rotation frequencies and surface inclination angles. The external field strength was kept constant at 10 mT for experiments involving this initial design. A paper surface within a dry environment was used for the majority of the characterization tests due to its challenging nature, where beneficial damping and buoyancy forces are minimal and friction forces are high. Additional performance tests were conducted in both water and silicone oil to gauge and characterize robot capabilities in fluid environments of varying viscosity.

Much like the geometric variants of the μTUM robot, several terrain geometries were also developed to see if the presence of curved surfaces, small inclined surfaces, and holes in the terrain would significantly affect the robot's performance (Fig. 5.1(b)). These terrain geometries include a pattern with cylindrical bumps, a honeycomb pattern, and a knurled pattern. They were fabricated with a Form 1+ SLA 3D printer (Formlabs) using standard Formlabs black resin (RS-F2-GPBK-04).

Additional tests were also performed using newer μTUM robots with improved magnetization on a conductive aluminum substrate. This was to provide more incline angle data for simulation validation purposes. Although the improved torque characteristics on the newer robots can help with minimum field strength requirements and fighting resistive effects, results for incline climbing and translational speed should be similar between the two design iterations in low-drag dry environments. Please note that a version of this chapter was previously published by Micromachines [72].
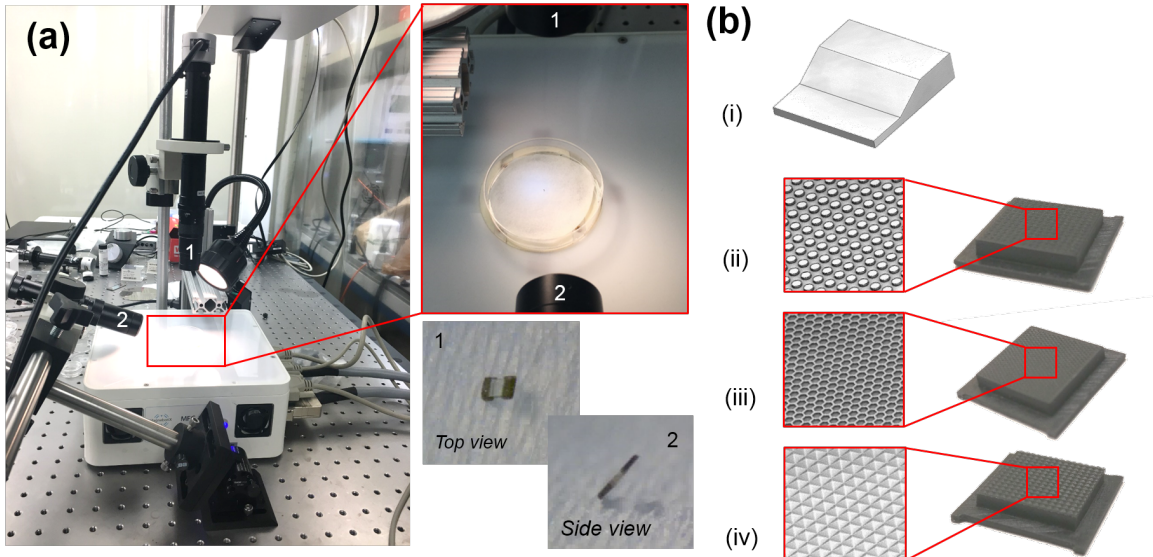
Figure 5.1. Experimental setup for mobility characterization tests. (a) The MFG-100 system with top camera (1) and side camera (2). The paper surface inside a petri dish at the center of the workspace. Top and side views of a μTUM as seen through the cameras. (b) Qualitative diagram of the various terrain geometries designed and fabricated: (i) inclined plane, (ii) cylindrical bumps, (iii) honeycomb, and (iv) knurled [72].

5.1 Experimental Setup

The driving external magnetic fields are generated by the MFG-100 system (MagnebotiX AG) as shown in Fig. 5.1(a). This system is capable of generating magnetic fields of over 20 mT in strength and field gradients of up to 2 T/m at the center of the workspace, which is about 10 mm in diameter. The power unit of the field generator can supply up to 20 A currents and uses eight coils at a time to generate the specified field or gradient in the workspace. Rotational fields of frequencies up to 2000Hz at 2mT and 100Hz at 8mT can also be generated in the workspace. The control software communicates with the electronics hardware to specify the field strength, gradient, and frequency of rotational fields in the workspace. This software can also control the yaw, roll, and pitch of the field's rotational axis, which allows for the steering control of μTUM robots. Real-time imaging is captured by an overhead camera and a side

camera aligned at 60° with the out of plane axis. CMOS cameras (Basler puA1600-60uc) along with microscope lenses (Edmund VZM 450i) of adjustable magnification are used in both the axes to record the motion of the robots.

5.2   Tumbling Locomotion Tests

5.2.1   Geometric Variations
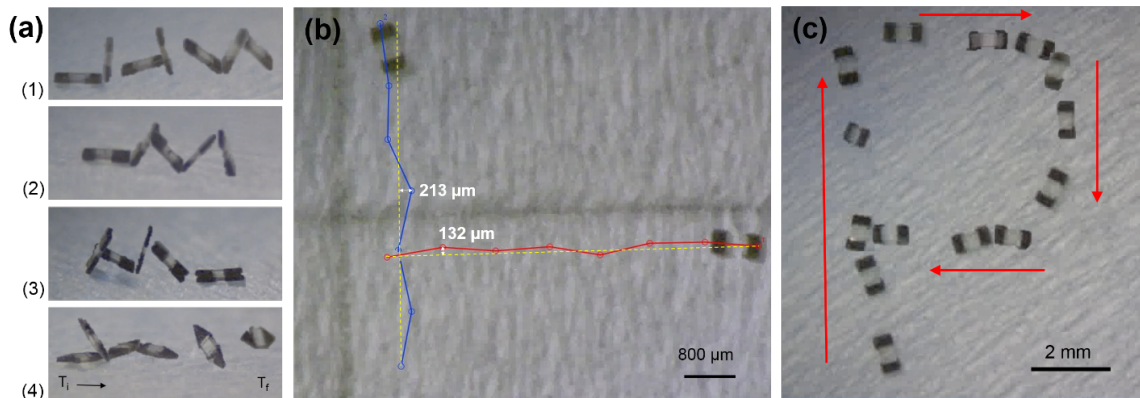
Figure 5.2. μTUM robot locomotion tests: flat paper substrate, dry environment, with 10 mT field strength at 0.5 Hz. (a) Images of trials for the μTUM robots with different end variations: (1) rounded rectangle, (2) asymmetric rounded rectangle, (3) rounded corners, and (4) triangle shape; (b) Trajectories (blue/red) of μTUM robot with respect to an ideal 5 mm long straight line trajectory (yellow); the maximum trajectory drift for each is reported.   (c) Rounded rectangle μTUM robot design traversing P-shaped trajectory [72].

The different geometric variants of the μTUM robots were tested for their tumbling locomotion capabilities along the same paper surface in dry environmental conditions (Fig. 5.2(a)). No significant differences were observed for robots with the rounded corners design and robots with the asymmetric variant of the default rounded rectangle design. However, the rounded corners robots were observed to be slightly faster than the default robots due to their longer length. Robots with the sharp corners design were also observed to be slightly faster than the default robots, but their corners had a tendency to hook into the fibers of the paper substrate. While this hooking action

may potentially be beneficial for climbing steep inclines, it is often detrimental and causes the robots to remain anchored to a particular spot. Robots with the triangle design were observed to be vertically unstable and frequently tilted over to their side. This behavior likely occurred because their centers of mass were not perfectly aligned with their endpoints. The result is that robots with the triangle robot design cannot maintain a stable tumbling motion and move forward in an erratic manner.

5.2.2 Open-Loop Directional Control

To assess the open-loop trajectory accuracy of the μTUM robot, the control rounded rectangular version was set to translate along a 5 mm long straight line path in both the vertical and horizontal directions. Fig. 5.2(b) shows these open-loop trajectories. The maximum deviations from the straight line paths were 213 μm and 132 μm for the vertical and horizontal tests, respectively.

The μTUM robot with the control rounded rectangle design was also demonstrated to be steerable along a desired trajectory. Manually adjusting the pitch and the yaw of the external field's rotational axis in increments of 90° allowed the robot to travel in a roughly P-shaped trajectory (Fig. 5.2(c)). The input was open-loop and no closed-loop control was implemented.

5.2.3 Translational Speed

Fig. 5.3 plots the average translational speed of a control μTUM robot under varying field rotational frequencies for a variety of environmental conditions. It can be seen that the translational speed of the robot in dry air on paper increases roughly linearly as the rotational frequency of the external field increases. Provided that the robot is tumbling without slipping, the resulting translational speed should be proportional to the length of its outer perimeter. This relationship can described in the following equation:
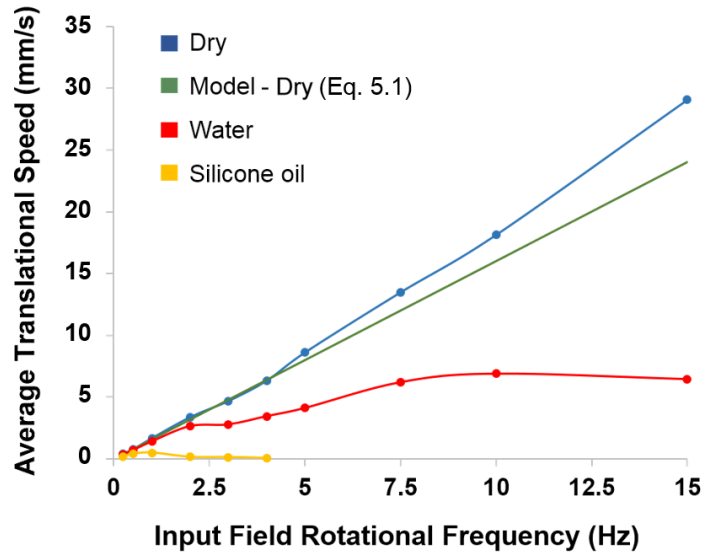
Figure 5.3. Experimental and modeled average translational speed under varying field rotational frequencies for various conditions [72].

$$v = 2(L + H)f_{rot} \tag{5.1}$$

While this model coincides with experimental results at lower frequencies, it can be seen that the experimental speeds are nonlinear and slightly higher than expected at higher frequencies. This discrepancy is likely because higher rotational frequencies can produce undesired magnetic field gradients in the MagnebotiX machine, which will apply a pulling force on the robot. A maximum translational speed of 24 mm/s was measured, but the upwards trend in Fig. 5.3 suggests that the speed of μTUM robot will continue to increase as the external field's rotational frequency increases above 15 Hz. On a substrate within a water environment, the presence of buoyancy forces lead to lower frictional forces, since friction is proportional to the total normal force. This reduced friction causes the μTUM robot to slip on the substrate, and the resultant relationship between the robot's translational speed and the field rotational frequency fails to follow a linear curve. At higher frequencies, the translational speed of the robot becomes noticeably saturated at 6.8 mm/s. On a substrate within a

silicone oil environment, higher viscosity and larger drag forces lead to phase lag between the orientation of the robot and the orientation of the external magnetic field. As the external field's rotational frequency increases, the larger drag forces prevent the μTUM robot from keeping up, and the robot begins oscillating in place instead of tumbling forward. This behavior occurs at field rotational frequencies of 2 Hz and above. Higher buoyancy forces in silicone oil result in even more slip, and the average translational speeds in this medium are much lower than in the others, with the maximum translational speed measured in silicone oil being 0.4875 mm/s.

5.2.4 Inclined Plane Climbing

Tests to determine if the control robot design could climb an incline at various angles were performed and evaluated on a pass/fail basis. The results are reported in Fig. 5.4(a). The dry air incline tests received more focus because the lack of beneficial buoyancy forces and the significant presence of electrostatic forces make the climb significantly harder. It was observed that the robot can go over a maximum inclination of 45° in dry conditions on paper. Due to the additional buoyancy force and dissipation of electrostatic charges in the denser liquid mediums, the robot was shown to be capable of climbing inclines of at least 60° in water and silicone oil. The possibility that the robot could be swimming was ruled out after it was observed that the robot did not move forward after losing contact with the surface. Fig. 5.4(b) shows images of the μTUM robot climbing up a 45° angle in dry conditions. It does not slip on the terrain in dry conditions until it reaches an incline angle that it cannot traverse. When the μTUM robot climbs inclines in either water or silicone oil, however, it tends to roll and slip along the incline, traveling at reduced overall speed.

5.2.5 Complex Terrain Traversal

Fig. 5.5 presents the robot's performance over various complex terrains. Tests were conducted on a flat paper surface and three 3D printed complex terrains, all

(a)

Incline Θ	Environment	Success? Y/N
5°	Dry	Y
10°	Dry	Y
15°	Dry	Y
30°	Dry	Y
45°	Dry	Y
60°	Dry	N
60°	Water	Y
60°	Silicone oil	Y

(b)

45°   500 μm
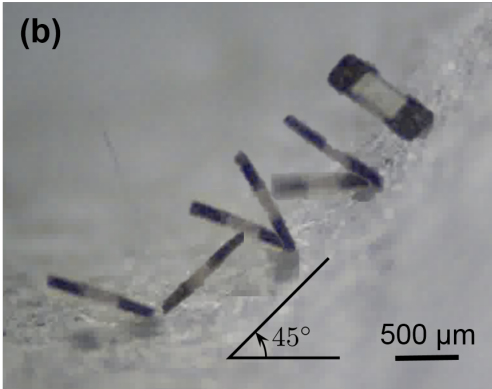
Figure 5.4. Inclined plane traversal tests. (a) Table of results for different inclination angles and environments; (b) Images of μTUM traversing a 45° angle in dry conditions (10 mT field @ 0.5 Hz) [72].

in dry conditions. Fig. 5.5(a) details the dimensions of each of the terrain features. Performance over the three complex terrains was similar, with mean velocities slightly slower than that of the flat surface. This can be attributed to the fact that the complex terrain surfaces bump or tilt the robot off to the side during the course of travel, as well as the difference in the difference in surface material.

Utilizing the default lengthwise tumbling mode, the robot was able to travel over the knurled and cylindrical bump terrains seen in Fig. 5.5(b)(ii) and Figure 5.5(b)(iii), respectively. However, it had difficulty getting up from its initial resting position on the honeycomb terrain. It is believed that concave pores, such as the honeycomb holes, increase the adhesive force between the robot and the surface when they are roughly the size of the robot's cross-sectional area. After switching the control μTUM robot with a robot configured for sideways tumbling, the honeycomb terrain became much easier to traverse, as seen in Fig. 5.5(b)(iv). With a smaller lever arm to rotate, the magnetic torque required to break the attractive surface forces decreased. The sideways tumbling μTUM robot variant, as a result, was able to traverse through honeycomb terrain under the same magnetic field strength and rotational frequency that the control lengthwise design could not.
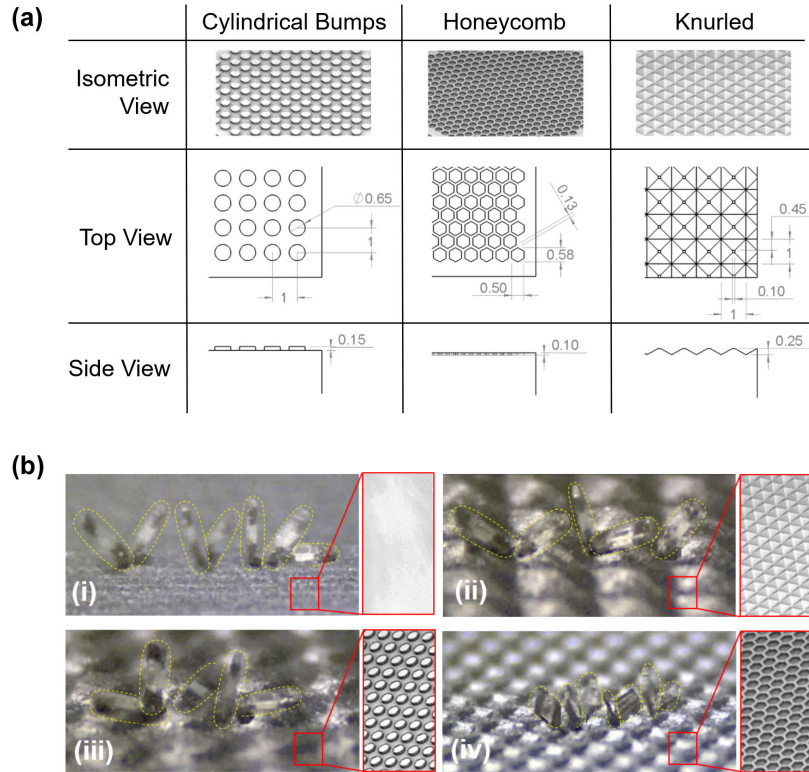
Figure 5.5. Terrain tests. (a) Dimensions of the terrain geometries explored (all dimensions in millimeters); (b) μTUM robots traveling over different terrains in dry environments, with 10 mT field strength @ 0.5 Hz. (i) Flat paper; (ii) cylindrical bumps; (ii) knurled surface; (iv) honeycomb terrain (side-ways tumbling mode) [72].

5.2.6 Discussion and Observations

The μTUM robot was able to exhibit tumbling movement through three different mediums under varying external field and surface conditions. As these environmental parameters were changed, several trends were observed. Increasing the drag coefficient of the surrounding environment limited the maximum field rotational frequency that the robot could follow. The dampened speeds observed in high-drag environments, however, also made the robot easier to observe and control. Increasing the density of the surrounding environment lowered the minimum field strength required to rotate the robot upwards from an initial resting position, due to larger buoyancy force. The reduced normal force between the robot and the surface, however, also reduced

friction force and made the robot more prone to slipping. In contrast, increased attractive forces between the robot and substrate raise the minimum field strength required for initial upwards rotation and make the robot less prone to slipping. In dry environments, the drag and buoyancy forces are both negligible, and high tumbling speeds can be obtained. This advantage occurs at the cost of high external field strength requirements, due to the presence of electrostatic attraction between the robot and the substrate. The opposite behavior is observed in wet environments, where the drag and buoyancy forces are both significant and electrostatic charges are dissipated into the fluid. The various trends that occur as the μTUM robot traverses through different environments presents challenges in closed-loop control and optimal pathfinding that will need to be addressed in the future.

The mobility characterization experiments demonstrate that highly viscous fluids, such as silicone oil, impose limitations on the robot's maximum rotational frequency, and low density mediums, such as air, impose limitations on the steepest incline that can be traversed, due to insignificant buoyancy forces. Minimizing slip, weight, and the effect of electrostatic charges is crucial for reducing the effect of these limitations and optimizing traversal through multiple terrains. There is a need to minimize the slip experienced by the outer edges of the robot while simultaneously avoiding the hooking action observed in robots with sharp corners. There is also a need to reduce the adhesive force on the main body of the robot. Options for making such improvements include increasing the robot's exterior surface roughness, increasing the contact area of its outer edges, and decreasing the contact area of the robot's main body.

Of the four different types of robot geometries fabricated, the rounded corners and rounded rectangle designs were the most effective at maintaining consistent forward movement. Excessively sharp corners were found to increase the likelihood of the robot hooking into rough surfaces and getting stuck. Decreasing the number of corners reduced vertical stability in dry conditions and tumbling motion could not be achieved for triangular end geometries. From the three different complex terrains fabricated,

it was observed that small concave surface features adversely affected the robot's performance by increasing the adhesion force between the robot and the substrate.

5.3   Simulated Tumbling Locomotion

5.3.1   Experimental Verification

To validate the finalized dynamic simulation model, the simulated results were compared against experimental results discussed earlier in this chapter.

All experimental results for the paper substrate material were obtained using the initial design iteration of the μTUM robot, with a non-magnetized midsection and error-prone magnetic alignment. The parameters for the robot used is listed in Table 5.1. While the robot has three distinct sections in this design variation, the simulation simplifies it down into a single, homogeneous block of uniform mass distribution. It can be argued that this assumption is acceptable at the microscale, where factors such as weight and inertia are much smaller in magnitude than factors proportional to distance and surface area, such as adhesion and electrostatic forces.

Experimental and simulation results for an additional aluminum substrate material are also included. This new material, which makes electrostatic forces negligible on conductive surface, was tested using a better-magnetized version of the μTUM robot (see Chapter 3) and provides further validation of the simulation model's results. The parameters for this robot and substrate are listed in Table 5.2.

Table 5.1.   Parameters for μTUM robot on paper [78].

Description	Value	Units
Mass (m)	1.6071×10^{-7}	kg
Electrostatic Force (F_{elect})	3.2022×10^{-6}	N
Friction Coefficient (μ)	0.3	-
Magnetic Alignment Offset (ϕ)	27	degree
Magnetic Volume (V_m)	2.9×10^{-11}	m^3
Magnetization ($|\boldsymbol{E}|$)	15000	A/m
Coefficient of adhesion force (C)	3.7148	N/m^2

Table 5.2. Parameters for improved μTUM robot on aluminum [78].

Description	Value	Units
Mass (m)	6.94×10^{-8}	kg
Electrostatic Force (F_{elect})	0	N
Friction Coefficient (μ)	0.54	-
Magnetic Alignment Offset (ϕ)	0	degree
Magnetic Volume (V_m)	3.2×10^{-11}	m^3
Magnetization ($|\boldsymbol{E}|$)	51835	A/m
Coefficient of adhesion force (C)	26.1771	N/m^2
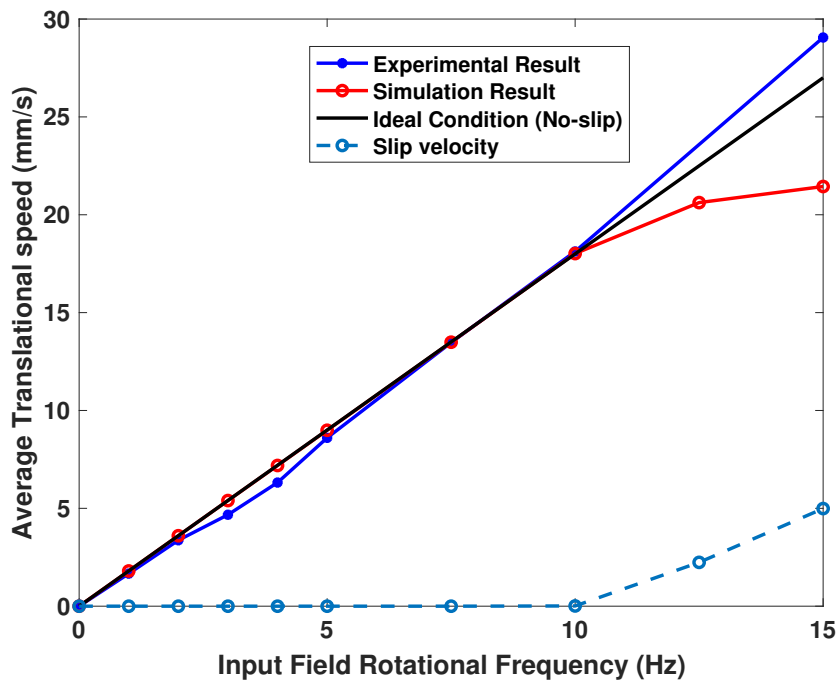
Figure 5.6. Tumbling locomotion tests on paper (20 mT field) [78].

Tumbling locomotion tests: The first scenario investigated was for tumbling locomotion of the μTUM traversing over a dry paper substrate. The parameters are, again, listed in Table 5.1. The simulation was set up to output the robot's translational speed on the substrate under varying field rotation frequencies. If the robot tumbles without slipping on the rough paper surface, the robot's average translational

speed, v, should again be approximately equal to two times the sum of body length and body height $(L + H)$ multiplied by the field rotational frequency f_{rot} (Eq. 5.1).

In these tests, the results of the robot in the experiments and the simulation can be compared with that of the ideal no-slip situation. In both cases, a rotating magnetic field of 20 mT was applied to the robot. Fig. 5.6 compares the experimental and simulation results with the ideal no-slip solution (Eq. (5.1)). When the frequency of rotating field increases, a discrepancy appears between the simulation results and the ideal solution. This discrepancy might occur because the robot starts slipping on the paper substrate under a high frequency rotational field. As shown in Fig. 5.6, the slip velocity increases as frequency increases, and its value is almost equal to the difference between ideal situation and simulation results. Thus, the discrepancy is likely due to slip velocity.

Again, the experimental results are observed to be slightly higher than expected because of complications in the MagnebotiX field generator. It is suspected that stray field gradients may become more prominent at higher rotational frequencies and pull the microrobot towards the edges of the workspace, causing it to move faster.

Table 5.3.   Results for inclined plane tests on paper (20 mT @ 1 Hz) [78].

Incline (θ)	Simulation (Y/N)	Experiment (Y/N)
5°	Y	Y
10°	Y	Y
15°	Y	Y
30°	Y	Y
45°	Y	Y
60°	N	N

Inclined plane traversal tests on paper: In the second scenario, the simulation is set up to determine whether the when the microrobot slips on an inclined surface (paper in dry conditions) at various angles. A 20 mT magnetic field rotating at a 1 Hz frequency was applied to the robot. Again, the simulation results were compared against the experimental results to validate the dynamic model. Based on
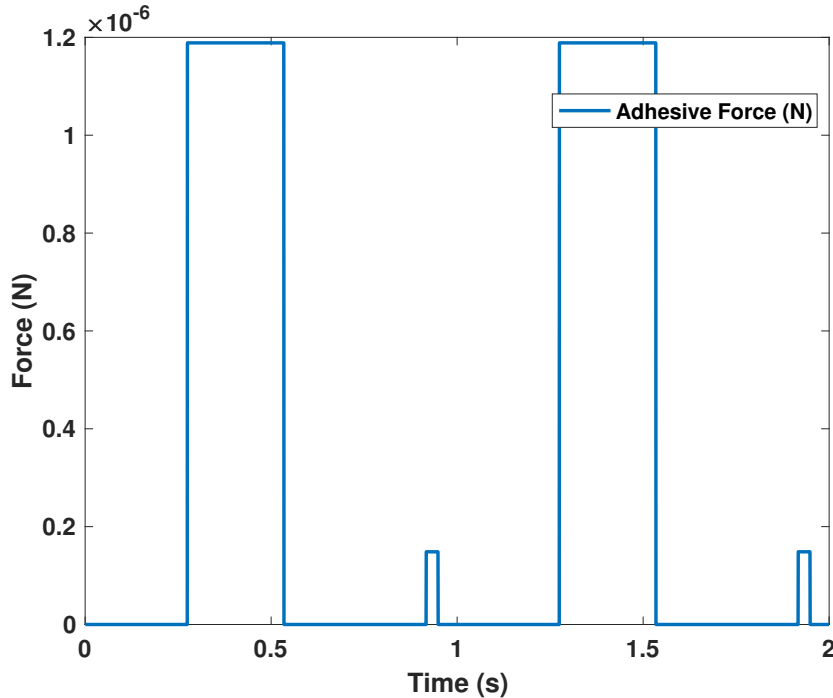
Figure 5.7. Simulation result for adhesive force acting on μTUM robot when it is tumbling over the incline (paper) of 45 degree (20 mT field @ 1 Hz) [78].

the experimental results, the robot can go over a maximum inclination of 45° on paper but it fails to climb a slope of 60°. The simulation output matches these results. Fig. 5.7 plots the adhesive force when robot is tumbling over the incline at 45°. It can be observed from this figure that the force changes periodically. When the contact area is large (Length $\times$ Width), the adhesive force reaches a value of $1.19e - 6N$. When the contact area is small (Width $\times$ Height), the adhesive force value goes to $1.49e - 7N$. In line contact cases, the adhesive force is almost zero.

Inclined plane traversal tests on aluminum: In the third scenario, the performance of a μTUM robot with improved magnetic properties was tested on an aluminum substrate, which is non-magnetic and conductive. As a result, no significant electrostatic forces or additional magnetic forces should have been applied on the robot during tumbling motion on this substrate. Although an electromagnetic drag force might have been exerted on the μTUM due to eddy currents induced in the

conductive aluminum, this force is estimated to be two orders of magnitude smaller than the magnetic torque and thus negligible. The coefficient of adhesive force on aluminum was found to be 26.18 N/m^2 and the coefficient of friction was found to be 0.54. A 20 mT magnetic field rotating at 1 Hz frequency was again applied to the robot. In both the simulations and the experiments, the robot could successfully climb an inclination of 30° but fails to climb 45°.

With several mobility results coinciding with the experimental results, it can be safely said that the dynamic simulation tool presented in Chapter 4 is valid for modeling and design purposes.

5.3.2   Optimal Design Prediction Using Simulation Tools

With the simulation model closely matching experimental results and validated, it can be used to explore alternative μTUM robot geometries for increased performance. As mentioned in Chapter 3, spiked shape robots, spiked ended robots, curved shape robots, and the control 'cuboid' shape robots were all simulated to explore the effect of the robots' design and dimensions on their performance. It was assumed that all the robots had the same inertia and magnetic properties, the same as those listed in Table 5.2.

The simulation includes both the tumbling locomotion tests and the inclined plane traversal tests from the previous sections. In the tumbling locomotion tests, a 20 mT rotational magnetic field rotating at 10 Hz frequency was applied to all the robots. Although these tests could have been performed at 1 Hz for consistency, this value was increased to 10 Hz in order to emphasize the velocity differences between the four designs due to slip. In Fig. 5.8, it can be observed that each robot's performance on paper is similar to its performance on aluminum. Furthermore, the curved shape robot was found to move the fastest while the cuboid shape robot moved the slowest. In the inclined plane traversal test, only the aluminum substrate was tested. All robots except the curved shape robot successfully climbed inclines up to 30° and failed at 45°.

Based on the simulation results, it can be concluded that the curved shaped robot has the best performance in terms of linear speed, but also the worst performance in terms of climbing ability. Additionally, it can be observed that the control 'cuboid' shape robot is not the best design for tumbling locomotion, but instead the spiked ended robot, with the best overall performance in both the locomotion tests and inclined plane tests.
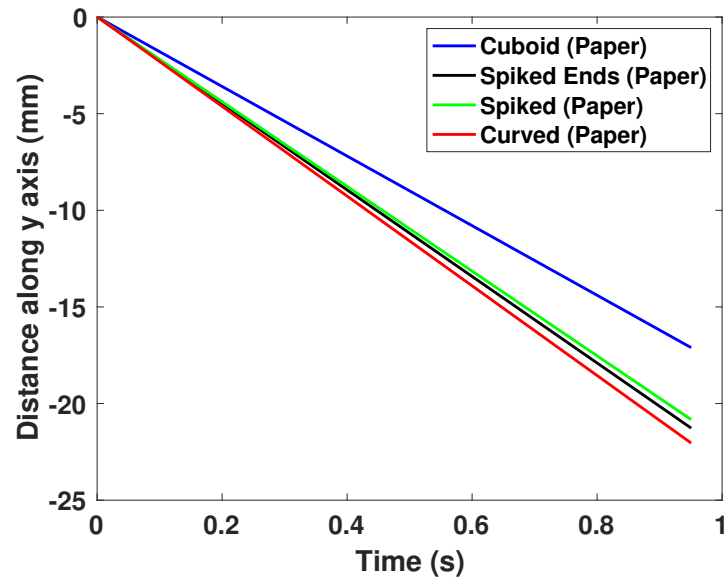
(a) Tumbling tests on paper.
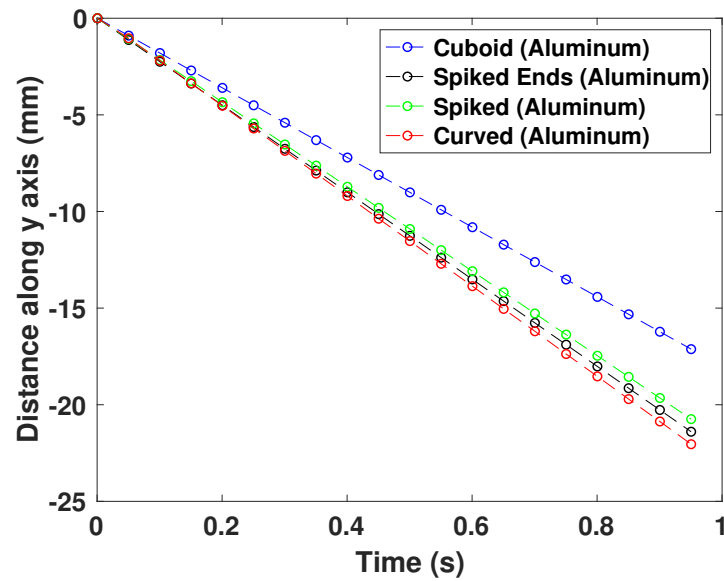
(b) Tumbling tests on aluminum.

Figure 5.8. Simulation result for robots with different geometric shapes: tumbling locomotion test (20 mT field @ 10 Hz) [78].

6. BIOMEDICAL APPLICATION EXPERIMENTS

The μTUM robot has a high ratio of magnetic volume relative to its overall size and is capable of traversing complex terrain in both wet and dry environments, making it an ideal choice for untethered experiments and biomedical applications within the body.

Of particular interest are colonoscopies, which are necessary to examine and diagnose colorectal cancer and inflammatory bowel disease. These two ailments affect millions worldwide and can cause fatigue, bloody diarrhea, weight loss, and abdominal pain [99]. Due to the invasiveness of the colonoscopy procedure, patients often experience extreme discomfort and reluctance to undergo further examination [100]. Additionally, colonoscopies themselves have the potential to exacerbate existing disease symptoms [101]. The use of ultra-thin colonoscopes has been shown to significantly improve tolerability in patients [102]. Non-invasive options such as bowel ultrasounds [103] and quantitative fecal immunochemical tests [104] also exist and can provide partial colon screening. Despite these options, no solution has fully eliminated the need for colonoscopies. The introduction of a microrobotic alternative, however, could lead to new non-invasive procedures that reduce patient discomfort and open new possibilities in disease diagnosis.

To explore this potential application, mobility of the μTUM robot is tested in *in vivo* murine colons and imaged in real-time using ultrasound technology. Payload diffusion and biocompatibility tests are also conducted to test the therapeutic efficacy and toxicity of the robot as well. Please note that a version of this chapter was previously published for the International Conference on Manipulation, Automation and Robotics at Small Scales (MARSS) [77].

6.1 Ultrasound Imaging

The real-time visualization of microrobot location is necessary for actively guiding non-autonomous microrobots in biomedical applications. For minimally invasive operations, the point of insertion of a microrobot will rarely coincide with the desired target location. Yet, *in vivo* microrobot imaging in cases where tissue occludes the line of sight has not been investigated extensively in literature. Though fluorescence imaging has been posed as a potential solution, the spatial resolution and frame rate of this method tends to be poor. Real-time imaging using ultrasound techniques is a promising alternative, and the high density of NdFeB particles in the μTUM robot offers enough contrast in acoustic impedance to appear distinct from its organic surroundings.

A drawback of ultrasound imaging is the phenomenon of acoustic shadowing, where gas bubbles and other materials with contrasting density can occlude objects below them. Additionally, ultrasound imaging captures a cross-sectional slice as opposed to an overhead view or 3D spatial view. It is crucial to position ultrasound sensor accurately and in a location where the sound waves will slice through the microrobot, which may be difficult due to its small size.

6.1.1 Experimental Setup

Real-time videos of the μTUM robot were acquired using a high-frequency ultrasound system (Vevo3100, FUJIFILM VisualSonics). A linear array ultrasound probe (MX700) with a frequency range of 30 to 70 MHz and a central frequency of 50 MHz was used to image C57BL/6 female apolipoprotein E ($apoE^{-/-}$) knockout mice at 12 weeks of age. A cylindrical NdFeB permanent magnet (1" diameter x 0.875" thick, Cyl1875, SuperMagnetMan) was rotated at a frequency of 1 Hz underneath the animal, applying torque on a microrobot inserted inside the animal's colon. The direction of the robot's movement can be changed by reversing the rotation of the magnet or changing its axis of rotation. Fig. 6.1 illustrates the imaging setup with
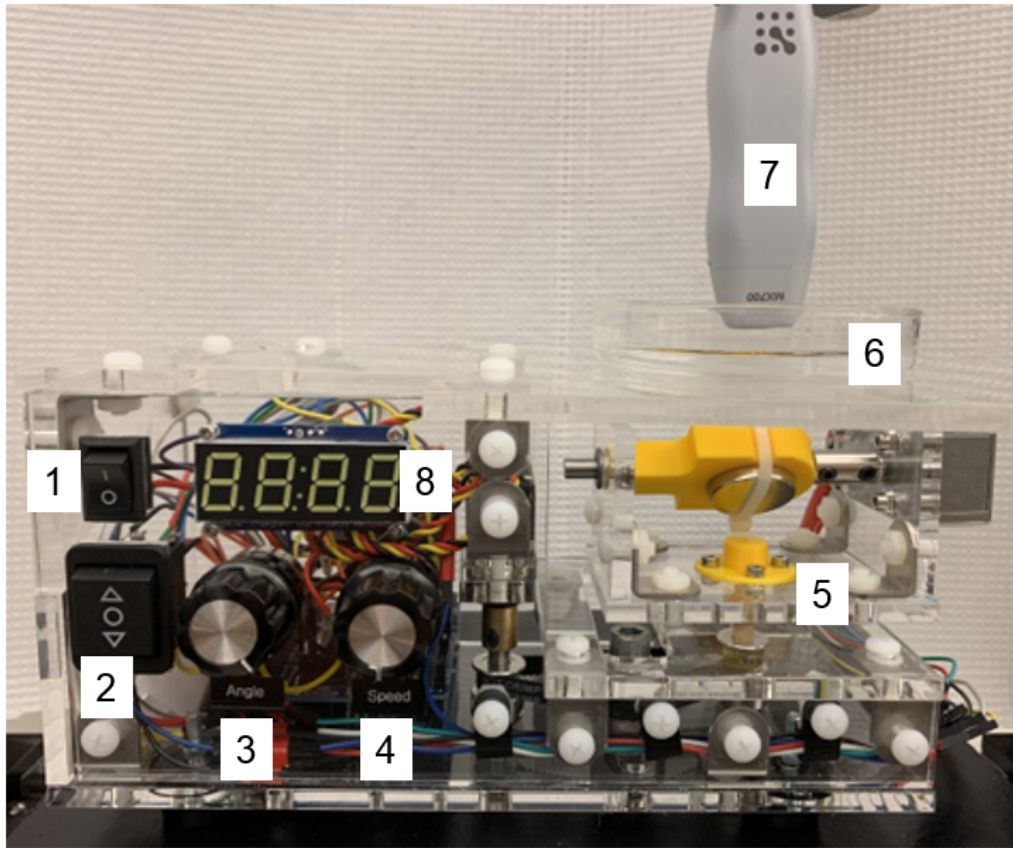
Figure 6.1. Experimental setup for ultrasound imaging with (1) On/off button. (2) Rocker switch for motor control. (3) Angle control knob. (4) Speed control knob. (5) Rotating magnet holder. (6) Petri dish with sample. (7) Ultrasound probe. (8) LED display.

the probe placed above the specimen and the magnet placed below it. Microrobot movement was tested for *in vitro*, *in situ* dissected, and *in situ* intact conditions. Average velocities, $\bar{v}$, were calculated for each condition using Eq. 6.1:

$$\bar{v} = \frac{\Delta x}{\Delta t} = \frac{x_f - x_0}{t_f - t_0} \tag{6.1}$$

where Δx represents the change in position, from the final position, x_f, to the initial position, x_0, and Δt represents the change in time, from the final timepoint, t_f, to the initial timepoint, t_0, as shown in Table 1 [105].

6.1.2   Portable Rotating Magnet System
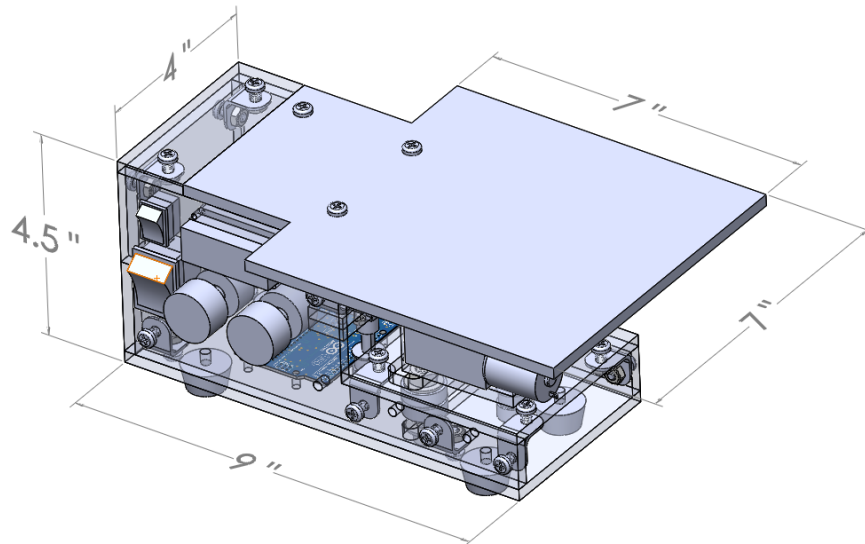
Figure 6.2.   CAD assembly of rotating magnet system with major dimensions in inches.

A custom system was designed and fabricated (Fig. 6.2-6.3) to manipulate the aforementioned permanent magnet in the ultrasound experiments, due to size and portability limitations for the MagnebotiX machine used in the previous chapter. Using the model presented in [106] and an estimated distance between the mouse colon and the magnet of 0.75 inches, the magnetic field strength at the location of the microrobot should be approximately 21.4 mT with this system, which is comparable to field magnitudes from the MagnebotiX machine. This system uses a number of non-magnetic parts, including a wooden shaft, nylon fasteners, and an acrylic frame to avoid resistive magnetic effects while the permanent magnet is in motion. Two rotational degrees of freedom are available for the magnet (Fig. 6.3(b)), with a 180° servo motor (Hitec 32645S HS-645MG) actuating the holder for the magnet and a geared 12V DC motor (JGY-371) rotating the magnet itself. Motor control is made possible with an on-board Arduino and a manually tuned PID controller. Magnet
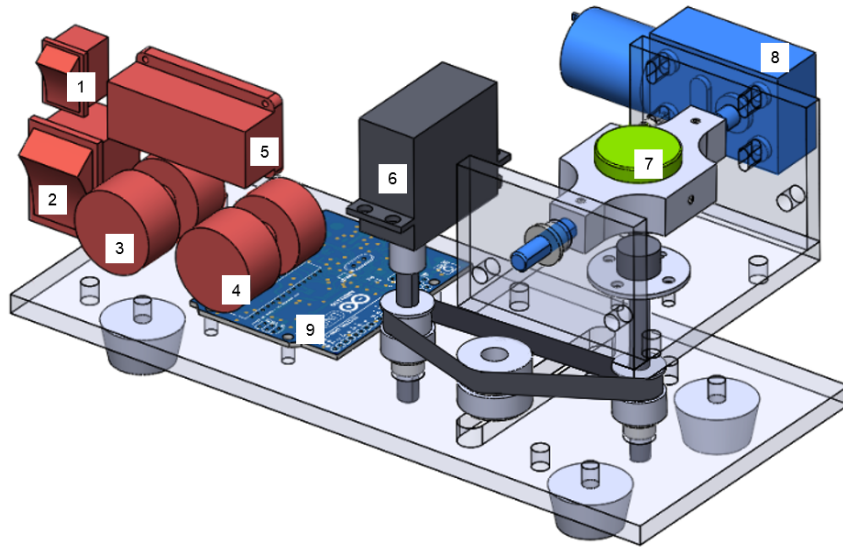
(a) Labelled cutaway of system with fasteners removed and key functional components highlighted: (1) On/off button. (2) Rocker switch for motor control. (3) Angle control knob. (4) Speed control knob. (5) LED Display. (6) 180° Servo Motor. (7) Permanent Magnet. (8) Geared DC Motor. (9) Arduino Board.
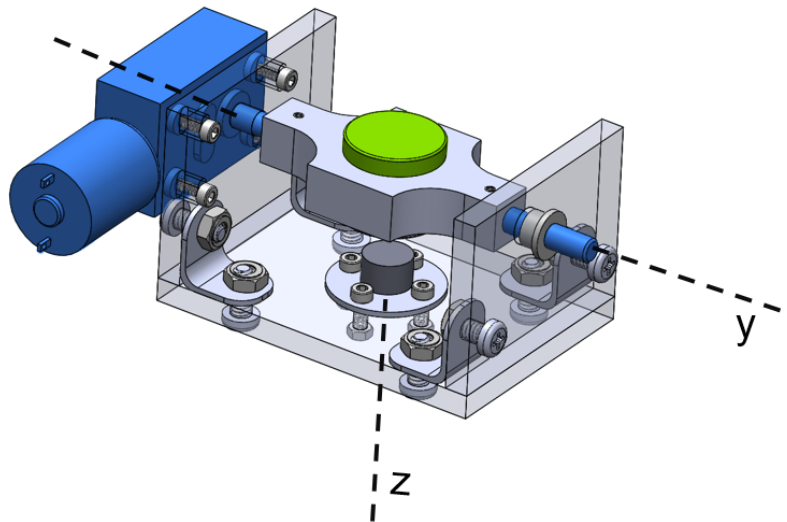
(b) Degrees of freedom for magnet system, with magnet holder exposed. Continuous 360° rotation is possible in the y-axis and reversible 180° rotation is possible in the z-axis.

Figure 6.3. Overview of portable rotating magnet system.

rotation frequencies can be set to either 0.5 Hz, 1 Hz, or 1.5 Hz, but only the 1 Hz option was used for the following experiments.

6.1.3 Locomotion
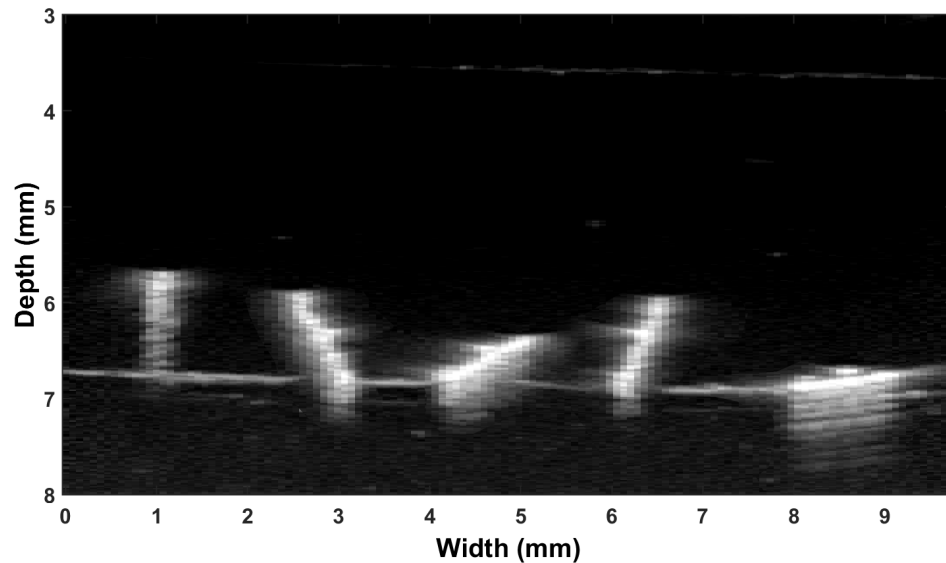
Figure 6.4. *in vitro* Tests: Ultrasound B-mode motion lapse of microrobot moving through water in a 1% agarose tube over a 4 second time period [77].

In Vitro Tests

The *in vitro* tests consisted of a 1% agarose gel block with a 3.175 mm in diameter hole traveling through the the block. A glass dish filled with water contained the agarose gel, and the robot was subsequently placed inside the hole. The magnet was rotated as B-mode images were acquired. Fig. 6.4 shows the microrobot traveling through the water-filled agarose tube at 2.2 mm/s.
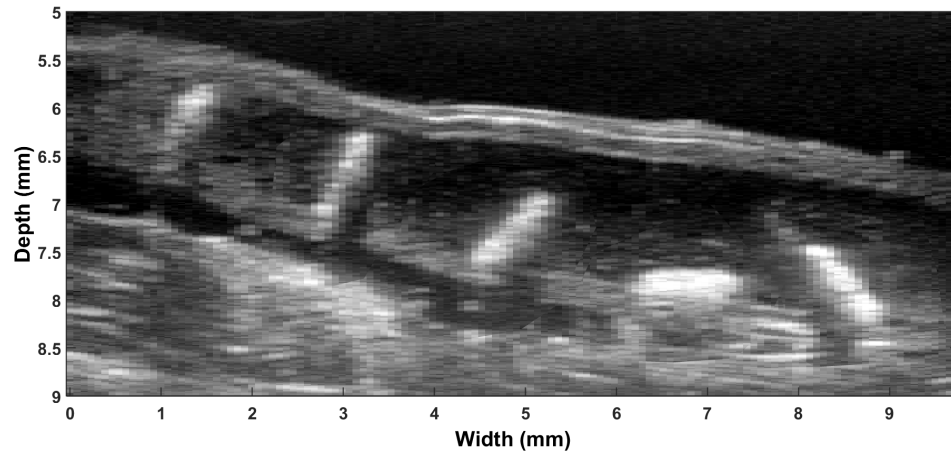
Figure 6.5. *in situ* Dissected Tests: Ultrasound B-mode motion lapse of microrobot traveling within the sutured off colon filled with saline over a 3 second time period [77].

In Situ Dissected Tests

For the *in situ* dissected tests, tissue anterior to the colon was removed and the robot was placed inside the colon of the mouse through the anus. The *in situ* tests involved filling the colon retrograde with solution and acquiring B-mode long-axis images of the mid and distal regions [107]. Saline was used as the solution for the dissected tests and the colon was subsequently sutured on both ends in order to ensure the liquid remained within the colon. This step was done to avoid the colon walls collapsing on the microrobot and preventing forward motion. Fig. 6.5 shows the microrobot traveling through the colon at roughly 1.9 mm/s.

In Situ Intact Tests

For the *in situ* intact tests, the tissue anterior to the colon was left in place while the robot was again inserted into the anus of the mouse. The colon was filled with a 1% Tylose solution [108] and the robot moved through the colon via the rotating magnet setup. This solution was much more viscous than water or saline, which allowed for the solution to support the shape of the colon without the need of other
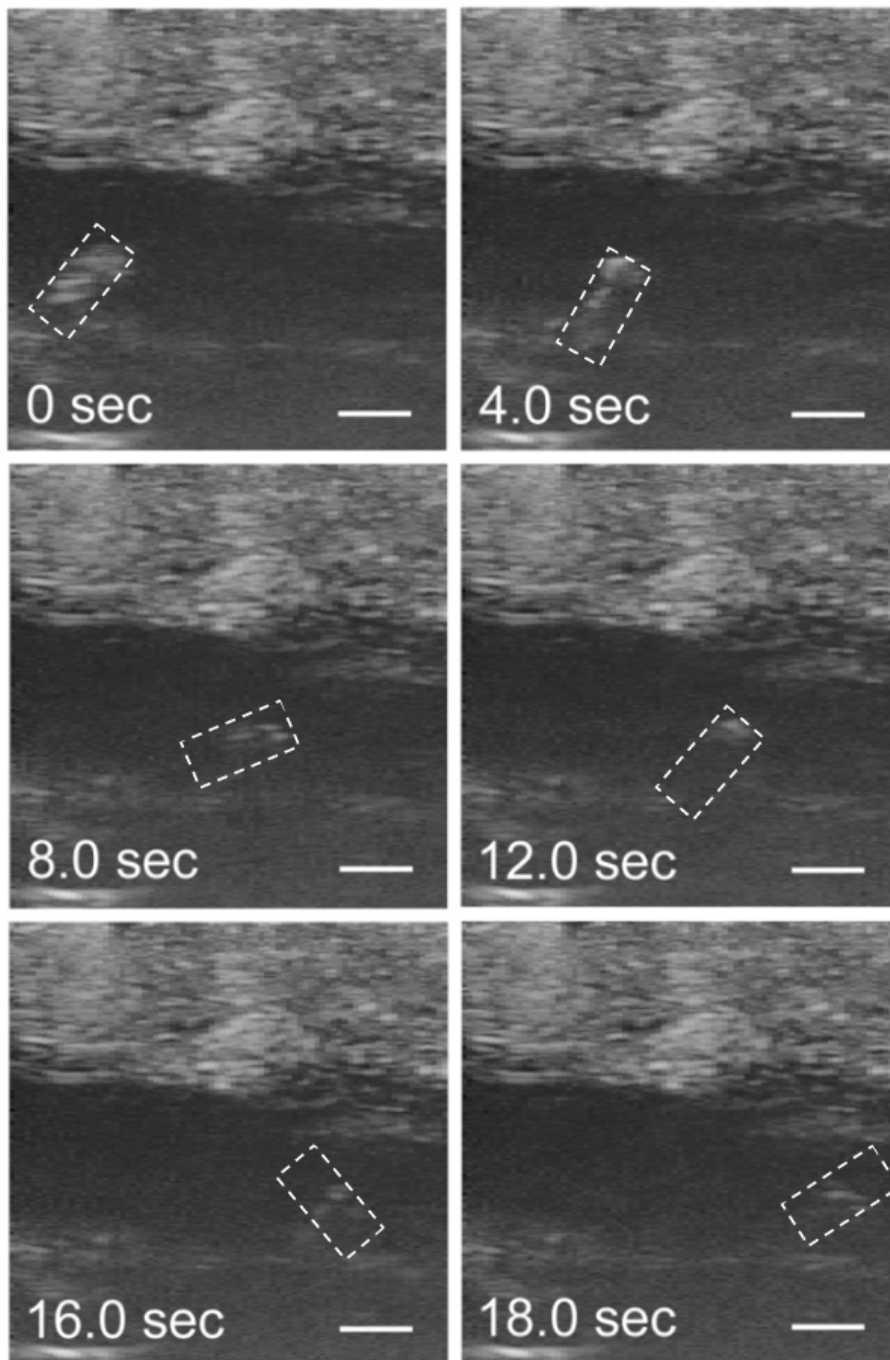
Figure 6.6. *in situ* Intact Tests: Ultrasound B-mode image sequence of microrobot traveling through a 1% Tylose solution in the colon over an 18 second time period. Scale bar is 1 mm [77].

constructs such as sutures. Solutions that are even more viscous than 1% Tylose, such as standard ultrasound gel, posed problems for microrobot movement. The viscous drag force overcomes the effect of gravity and the robot cannot reach the surface of the colon for traction. Within these viscous substances, the robot has difficulty translating along the length of the tissue. Fig. 6.6 displays the robot moving through the colon at roughly 0.2 mm/s.

In Vivo Intact Tests

For the *in vivo* intact tests, all tissue was left in place and the robot was directly inserted into the anus of the live mouse. The colon was first filled with ultrasound gel and then flushed out to remove any obstructing fecal matter inside. Afterward, it was filled with saline and a clothespin was used at the rectum to prevent the saline from spilling out. Similar to [109], the mouse was treated with a subcutaneous 0.02 mg/mL, 100-150 μL atropine injection (#A0132, Sigma-Aldrich) about 5 minutes prior to the imaging session to halt peristaltic contractions that could block or compress the colon. Fig. 6.7 displays the robot moving through the colon at roughly 2.1 mm/s.

6.1.4   Discussion and Observations

As shown in Table 6.1, the velocities varied greatly among the different conditions. The aqueous *in vitro* tests had the largest velocity, the *in situ* dissected and *in vivo* intact experiments in saline had a slightly smaller velocity, and the *in situ* intact tests in 1% Tylose demonstrated the smallest velocity. This is likely due to the differences in viscosity of the solutions as well as differences in the terrain of the test environment. Though not the only factor determining the resultant velocities, viscous drag played a major role in the differences between tests. The 1% Tylose solution is much more viscous than the aqueous environments used in the other tests. While the viscosity of water is about 0.89 mPa·s, the 1% Tylose solution is more viscous at a value of 4500 mPa·s [110]. The environment of each test also needs to be accounted for, with
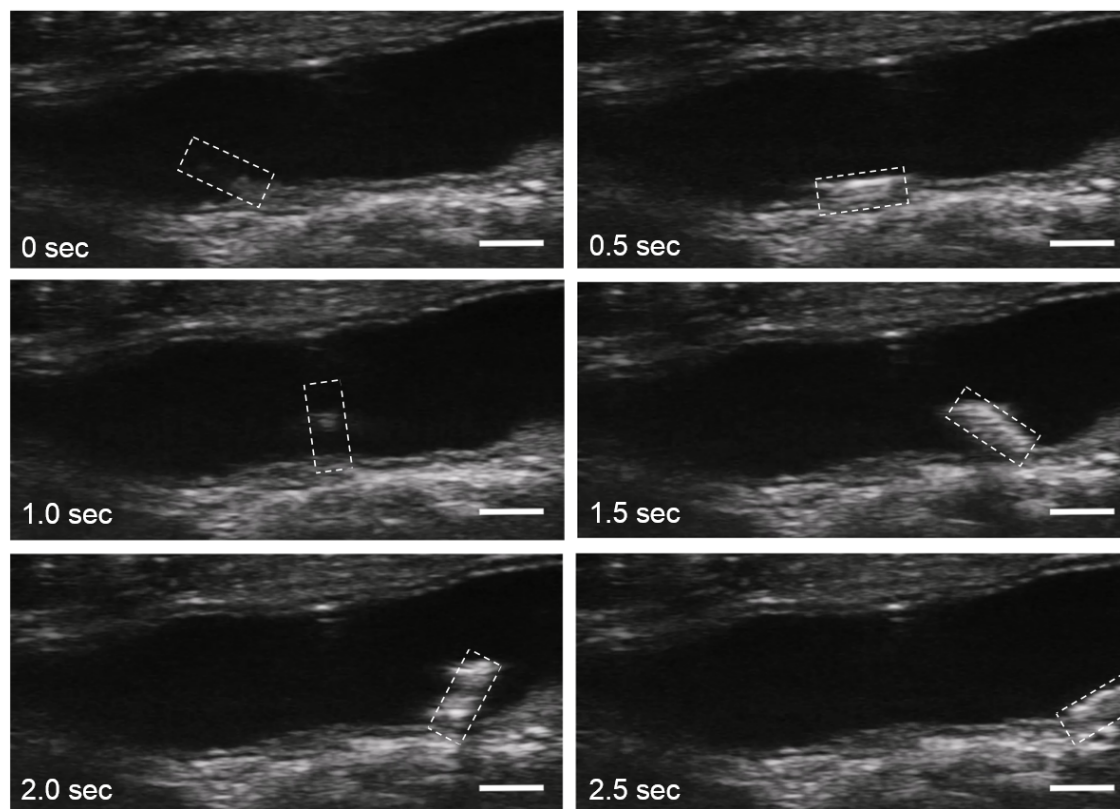
Figure 6.7. *in vivo* Intact Tests: Ultrasound B-mode image sequence of microrobot traveling through a saline solution in the colon over a 2.5 second time period. Scale bar is 1 mm.

differences in the heterogeneity of the terrain and the coefficient of friction. These differences result in variations in the robot's ability to grip the substrate surface, travel across the surface, and travel through the surrounding solution. The standard deviations in velocity were found to be greater in the *in situ* and *in vivo* tests than the *in vitro* tests. This makes sense because the *in vitro* tests provide a homogeneous surface for the robot, while the *in situ* and *in vivo* tests had a varying surface down the length of the colon. To summarize, the microrobot maintained its ability to move through a wide variety of *in vitro*, *in situ*, and *in vivo* conditions, albeit with varying levels of success, and could be observed in real-time using ultrasound imaging techniques.

Table 6.1. Microrobot velocities in different test conditions [77].

Test Condition	Water *in vitro*	Saline *in situ* dissected	1% Tylose *in situ* intact	Saline *in vivo* intact
Trial 1 (mm/s)	2.23	1.96	0.19	2.12
Trial 2 (mm/s)	2.21	1.89	0.19	2.03
Trial 3 (mm/s)	2.23	1.87	0.25	2.06
Average Velocity (mm/s)	2.23	1.91	0.21	2.06
Standard Deviation (mm/s)	0.01	0.05	0.04	0.05

6.2 Payload Diffusion

The diffusion characteristics of a fluorescent payload coating the microrobot were quantified to explore targeted drug delivery applications. The microrobots were coated with a PLGA solution consisting of N-methyl pyrrilidone (NMP), poly(lactic-co-glycolic acid) (PLGA), and fluorescein. The coated microrobots were then placed into 1 mL of phosphate buffered saline (PBS) in a 2 mL serum vial. These were kept at 37°C on a shaker at 100 rpm. Samples were taken from the bath-side solution at 0.25, 0.5, 1, 2, 4, 6, 24, 48, 96, and 120 hours after initial coating. The bath
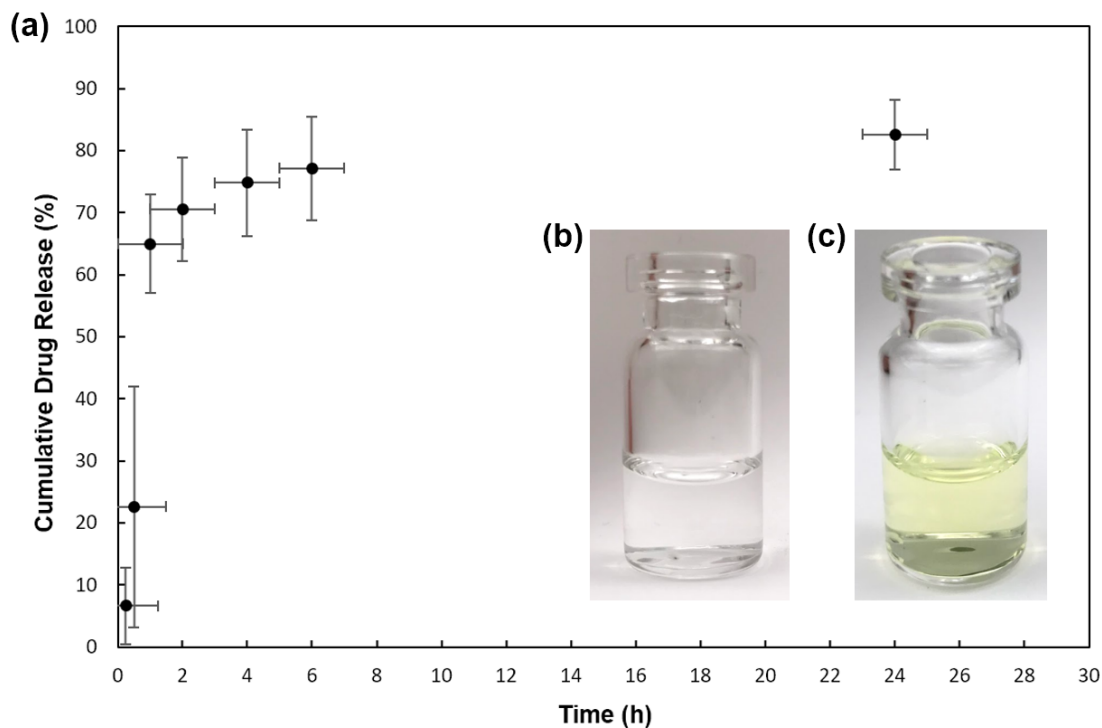
Figure 6.8. Payload diffusion tests. (a) Cumulative mass data of diffusion study (for the first 24 hours). (b) Microrobot initially placed in glass vial. (c) Microrobot in vial and PBS 24 hours later. Green solution is fluorescein released from PLGA coating [77].

solution was replaced with fresh PBS at all sampling time points to maintain conditions. After 168 hours (7 days), the coated microrobots were dissolved in NaOH to determine any residual drug mass. The fluorescence of each sample was quantified afterwards using a SpectraMax M5 microplate reader. The samples were read at an excitation wavelength of 485 nm and emission wavelength of 525 nm. The results shown in Fig. 6.8 were obtained by comparing experimental measurements against a standard curve of absorbance values, which itself was generated by making solutions with known fluorescence concentrations. The experiment was ran in triplicate to reduce the possibility of experimental bias or random error. It can be observed that most of the payload diffuses within the first two hours of resting in the PBS bath. This should be a sufficiently long time for the microrobot to travel from desired point of entry in the body to a nearby target location.

6.3 Biocompatibility

To assess the short-term cytotoxicity of the doped SU-8 used to fabricate the microrobots, the cell viability of NIH3T3 murine fibroblasts in direct contact with the materials was studied over the course of three days, with day 0 measurements taken 12 hours after initial seeding. The NIH3T3 fibroblasts were seeded on surfaces of both SU-8 and SU-8 with NdFeB particles, and were compared to negative and positive controls consisting of tissue culture polystyrene and cells cultured in 70% ethanol, respectively, to elicit a cytotoxic response. Proliferation was examined using fluorescence microscopy (BioTek Cytation5 Cell Imaging Multi-Mode Reader). Fig. 6.9 indicates cell proliferation on doped SU-8 and the cells do not exhibit signs of short-term toxicity. This result is optimistic for the overall biocompabitility of the μTUM robot. As expected, the negative control experienced cell proliferation while the positive control had no living cells after three days. Doped PDMS was tested as well, but the results were similar to that of the positive control. This is likely because the toxic solvent used in the photoresist's curing process was not fully removed before testing.
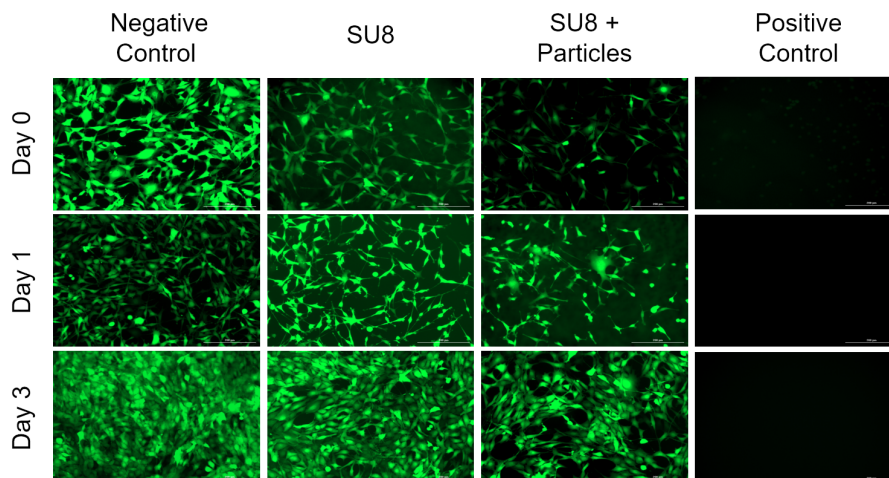
Figure 6.9. Fluorescent images taken of cell proliferation for four different test cases. Green fluorescent cells indicate living cells that have adhered to the well plate and are viable [77].

7. CONCLUSION

7.1 Summary

To conclude, the mobility and biomedical applications of a microscale magnetic tumbling robot capable of traversing complex terrains in dry and wet environments were explored. A flexible fabrication method using standard photolithography techniques and SU-8 photoresist doped with NdFeB was developed, allowing for configurable magnetic alignment regardless of physical geometry. The strong magnetization of the NdFeB robot allowed for locomotion at magnetic field strength magnitudes as low as 3 mT. Static force analysis of the robot and dynamic modeling of its motion characteristics were performed with experimental verification. The resultant dynamic model was capable of simulating intermittent contact with a surface area-dependent adhesion force. Multiple geometric variations were simulated and it was predicted that a μTUM robot with spiked ends would move faster and climb higher inclines than the basic rectangular design. The microrobot was shown to move over several materials in both dry and wet conditions, including paper, aluminum, and murine colon tissue. In dry environments, the robot can move at translational speeds in excess of 24 mm/s, though in wet environments this speed was limited to approximately 6.8 mm/s. The robot can climb inclines of up to 60° and can move over complex, unstructured terrain as well. The outer surface of the robot can be functionalized for various biomedical applications towards treating NCD's. It is well-posed for *in vivo* operations, demonstrating the ability to diffuse a payload slowly over two hours and being biocompatible with murine fibroblasts. When visually occluded inside a live murine colon, the microrobot was still able to move and its real-time position could be tracked using high-resolution ultrasound imaging. The overall capabilities of the

tumbling microrobot make it promising for targeted drug delivery and other *in vivo* biomedical applications.

7.2 Future Work

7.2.1 Further Variation of Dynamic Simulation Parameters

The dynamic simulation model discussed in Chapter 3 was used as a tool for finding an optimal design between several geometries, including a rectangular 'cuboid' shape, a spiked shape, a spiked ended shape, and a curved shape. However, only one variation of each of these geometries was simulated and compared against the others. In future studies, the depth of the optimization process can be expanded by varying the dimensions in each distinct geometry. The size of the spikes or the radius of the curve, for example, can be changed to significantly alter the resultant mobility characteristics of the robot. Afterwards, the optimized microrobot design can be fabricated to validate and verify the improved performance predicted by the simulation.

7.2.2 Soft-Body Magnetic Microrobot With Non-Uniform Alignment

Many small organisms in nature are soft-bodied and capable of bending, stretching, and deforming reversibly. This helps them move through unstructured environments and adapt to difficult terrain. In its current rigid body state with uniform magnetic alignment, the μTUM robot lacks the same abilities and is only capable of two locomotion modes: tumbling and sliding (through magnetic field gradients). By combining a flexible photoresist material with a low modulus of elasticity, such as PDMS, and magnetizing the robot non-uniformly, it is possible to get around these limitations. Hu et al. demonstrated these two improvements to great effect with their magneto-elastic millimeter-scale robots, which were capable of mimicking crawling, swimming, and jumping motions among other things [43]. Much like a worm or a

grasshopper, these robots were able to squeeze through tight spaces and hop onto steep ledges. They could swim three dimensionally like a jellyfish and break through the effects of surface tension on a water-air interface. The flexible NdFeB robots were magnetized while they were wrapped around a glass rod, leading to a sinusoidal-like magnetization once released. In the presence of varying magnetic field strengths, they could curl inward and undulate cyclically. By precisely controlling the external magnetic field's strength, direction, and gradients, it was possible to manipulate this unique behavior in many different locomotion modes. Miniaturizing the milli-robot's fabrication method to the microscale has yet to be done, but soft-bodied, biomimetic microrobots will certainly be an important research direction for the future.

7.2.3 Improved Roll-to-Roll Fabrication Method

Currently, the μTUM robot fabrication process involves some steps that are time-consuming and require manual intervention. The robots are released from wafers by hand after being cured and sometimes come off chipped or in pieces. Additionally, inserting and removing samples from the PPMS machine for magnetization is a tedious process, where robots must be attached to the sample holder by hand and only limited numbers can be attached at one time. The adhesive used to attach the robots to the sample holder is sometimes difficult to remove and can damage the robot as well. The manual steps in the μTUM robot's fabrication process introduce room for error and limit the rate at which the robots can be produced at scale. Roll-to-roll manufacturing processes may improve the current fabrication method by performing fabrication in an assembly-line fashion. NdFeB-doped polymers can be cured as a large sheet, then magnetized in parts over a moving conveyor, and finally laser cut en masse into the desired two dimensional geometry. Such a process would allow hundreds of microrobots to be fabricated at once, greatly increasing throughput.
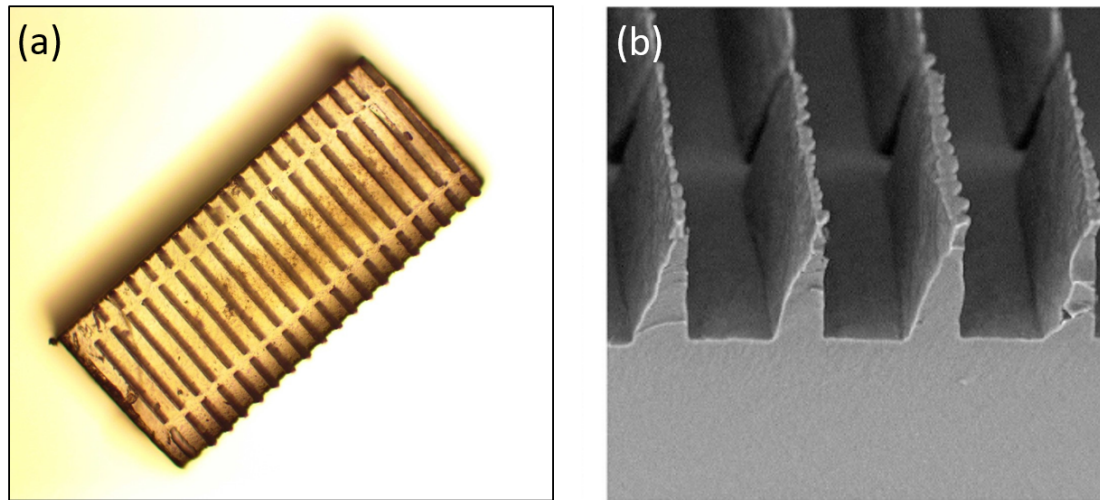
Figure 7.1. PDMS 'gecko' feet (a) Microscope image of laser-cut 'gecko' PDMS layer cut in the dimensions of the μTUM robot (b) Scanning electron microscope close-up image of 'gecko' feet side profile with protruding stalks from [111].

7.2.4 Improved Mobility With 'Gecko' PDMS Feet and Adhesive Coating

Modabberifar et al. demonstrated a macroscale robotic gripper that could reversibly grasp and release flat, smooth surfaces without the use of chemical adhesives [111]. This ability was accomplished using PDMS pads at the end of the grippers that were actuated with contracting shape-memory alloy (SMA) wires. These compliant PDMS pads contained molded microscale stalks that resembled the structures observed on the feet of geckos 7.1(b). When pulled in shear by the SMA wires, the stalks on the pads bend against the surface and increase the contact area between the gripper and the surface. The increased contact area causes adhesion to increase as well, allowing the robot to cling on to the flat surface.

Though the μTUM robot can not apply the same magnitude of force as the SMA wires (on the micro-Newton scale instead of the Newton scale), the 'gecko'-like PDMS structures were still thought to be useful for two reasons: (1) elevating the robot off the ground and reducing contact area, decreasing the amount of magnet torque required to overcome adhesion forces, and (2) adding compliant structures to the edges of the

rigid robot, increasing traction and reducing slip on smooth/inclined surfaces. Thus, PDMS structures were layered on two opposite sides of the μTUM robot and excess material was removed with high-resolution laser cutter 7.1(a). When tested, these altered robots were able to operate at lower field strength magnitudes and could also overcome surface tension effects with greater ease. Additionally, it was observed that the 'gecko' μTUM robots could sometimes climb vertical surfaces if electrostatic forces on the underlying substrate were high enough. These electrostatic forces, however, are very difficult to quantify and precisely control, fluctuating significantly over the substrate and from changes in local humidity. If a device were developed to harness these forces, capable of activating and deactivating them on command, then vertical and upside-down climbing for the μTUM robots may be an interesting future research direction.

7.2.5   Machine Vision and Closed Loop Control

All of the experiments discussed in this work were carried through using open loop control and manual input for the actuating magnetic fields. In the future, an automated control system should be implemented to reduce human error, enhance path-planning decisions, and increase the speed that the robot can reach its target. This system is possible with an off-board computer that sends output based on machine vision input of the microrobot. Such real-time closed-loop feedback control is difficult for the μTUM robot when the MagnetbotiX machine is used as the external magnetic field source. For this machine, field parameters must be inputted through a MATLAB software interface, which adds additional computational overhead that significantly increases processing time beyond real-time thresholds. With the Arduino-powered permanent magnet manipulator, however, it is possible to use a different interface to control the actuating magnetic field. Real-time control using this setup should be considered and explored for future studies.

Due to the largely uniform nature of the magnetic fields used for actuation, all identical magnetic microrobots will behave the same way under the global fields. This is problematic for swarm control, where it is more than often advantageous to have multiple robots performing different actions and traveling in independent directions at the same time. Though several works have addressed this independent control problem with solutions such as slight changes in geometry between individual robots for selective control [112] and arrays of microcoils for simultaneous independent actuation [113], it remains another issue that needs further answers before truly intelligent microrobot adaptation and control can be realized.

REFERENCES

REFERENCES

[1] Max Roser. Life Expectancy. https://ourworldindata.org/life-expectancy, 2019.

[2] James C Riley. Estimates of Regional and Global Life Expectancy, 18002001. *Population and Development Review*, 31(3):537–543, 2005.

[3] Deaths from NCDs: Situation and Trends. https://www.who.int/gho/ncd/mortality morbidity/ncd total/en/, 2019.

[4] Cancer Treatments — CancerQuest. https://www.cancerquest.org/patients/treatments.

[5] Miriam Krischke, Georg Hempel, Swantje Völler, Nicolas André, Maurizio D'Incalci, Gianni Bisogno, Wolfgang Köpcke, Matthias Borowski, Ralf Herold, Alan V Boddy, and Joachim Boos. Pharmacokinetic and pharmacodynamic study of doxorubicin in children with cancer: results of a "European Pediatric Oncology Off-patents Medicines Consortium" trial. *Cancer chemotherapy and pharmacology*, 78(6):1175–1184, dec 2016.

[6] Leo M. L. Nollet and Leen De Gelder. *Handbook of Water Analysis*.

[7] Lutz Alder, Kerstin Greulich, Günther Kempe, and Bärbel Vieth. Residue analysis of 500 high priority pesticides: better by GC-MS or LC-MS/MS? *Mass spectrometry reviews*, 25(6):838–65.

[8] Hakan Ceylan, Joshua Giltinan, Kristen Kozielski, and Metin Sitti. *Mobile microrobots for bioengineering applications*, volume 17. Royal Society of Chemistry, 2017.

[9] Metin Sitti, Hakan Ceylan, Wenqi Hu, Joshua Giltinan, Mehmet Turan, Sehyuk Yim, and Eric Diller. Biomedical Applications of Untethered Mobile Milli/Microrobots. *Proceedings of the IEEE. Institute of Electrical and Electronics Engineers*, 103(2):205–224, feb 2015.

[10] Pelin Erkoc, Immihan C. Yasa, Hakan Ceylan, Oncay Yasa, Yunus Alapan, Metin Sitti, Oncay Yasa, Metin Sitti, Pelin Erkoc, Immihan C. Yasa, and Hakan Ceylan. Mobile Microrobots for Active Therapeutic Delivery. *Advanced Therapeutics*, 2(1):1800064, jan 2018.

[11] Yabin Zhang, Ke Yuan, and Li Zhang. Micro/Nanomachines: from Functionalization to Sensing and Removal. *Advanced Materials Technologies*, 4(4), apr 2019.

[12] E. M. Purcell. Life at low Reynolds number. *American Journal of Physics*, 45(1):3–11, jan 1977.

[13] Walter F. Paxton, Kevin C. Kistler, Christine C. Olmeda, Ayusman Sen, Sarah K. St. Angelo, Yanyan Cao, Thomas E. Mallouk, Paul E. Lammert, and Vincent H. Crespi. Catalytic nanomotors: Autonomous movement of striped nanorods. *Journal of the American Chemical Society*, 126(41):13424–13431, oct 2004.

[14] Wei Gao, Sirilak Sattayasamitsathit, Jahir Orozco, and Joseph Wang. Highly efficient catalytic microengines: Template electrosynthesis of polyaniline/platinum microtubes. *Journal of the American Chemical Society*, 133(31):11862–11864, aug 2011.

[15] Xing Ma, Anita Jannasch, Urban Raphael Albrecht, Kersten Hahn, Albert Miguel-López, Erik Schäffer, and Samuel Sánchez. Enzyme-Powered Hollow Mesoporous Janus Nanomotors. *Nano Letters*, 15(10):7043–7050, oct 2015.

[16] Fangzhi Mou, Chuanrui Chen, Huiru Ma, Yixia Yin, Qingzhi Wu, and Jianguo Guan. Self-propelled micromotors driven by the magnesium-water reaction and their hemolytic properties. *Angewandte Chemie (International ed. in English)*, 52(28):7208–12, jul 2013.

[17] Wei Gao, Aysegul Uygun, and Joseph Wang. Hydrogen-bubble-propelled zinc-based microrockets in strongly acidic media. *Journal of the American Chemical Society*, 134(2):897–900, jan 2012.

[18] Ming Luo, Youzeng Feng, Tingwei Wang, and Jianguo Guan. Micro-/Nanorobots at Work in Active Drug Delivery. *Advanced Functional Materials*, 28(25), jun 2018.

[19] Ouajdi Felfoul, Mahmood Mohammadi, Louis Gaboury, and Sylvain Martel. Tumor targeting by computer controlled guidance of Magnetotactic Bacteria acting like autonomous microrobots. In *2011 IEEE/RSJ International Conference on Intelligent Robots and Systems*, pages 1304–1308. IEEE, sep 2011.

[20] Morgan M. Stanton, Juliane Simmchen, Xing Ma, Albert Miguel-López, and Samuel Sánchez. Biohybrid Janus Motors Driven by Escherichia coli. *Advanced Materials Interfaces*, 3(2), jan 2016.

[21] Veronika Magdanz, Samuel Sanchez, and Oliver G. Schmidt. Development of a sperm-flagella driven micro-bio-robot. *Advanced Materials*, 25(45):6581–6588, dec 2013.

[22] Chuanrui Chen, Fangzhi Mou, Leilei Xu, Shaofei Wang, Jianguo Guan, Zunpeng Feng, Quanwei Wang, Lei Kong, Wei Li, Joseph Wang, and Qingjie Zhang. Light-Steered Isotropic Semiconductor Micromotors. *Advanced Materials*, 29(3), 2017.

[23] Jean Pierre Abid, Michel Frigoli, Robert Pansu, Jacob Szeftel, Joseph Zyss, Chantal Larpent, and Sophie Brasselet. Light-driven directed motion of azobenzene-coated polymer nanoparticles in an aqueous medium. *Langmuir*, 27(13):7967–7971, jul 2011.

[24] Mingjun Xuan, Zhiguang Wu, Jingxin Shao, Luru Dai, Tieyan Si, and Qiang He. Near Infrared Light-Powered Janus Mesoporous Silica Nanoparticle Motors. *Journal of the American Chemical Society*, 138(20):6492–6497, may 2016.

[25] Xiuhui Wang, Jingchao Li, Naoki Kawazoe, and Guoping Chen. Photothermal Ablation of Cancer Cells by Albumin-Modified Gold Nanorods and Activation of Dendritic Cells. *Materials (Basel, Switzerland)*, 12(1), dec 2018.

[26] Kwanoh Kim, Xiaobin Xu, Jianhe Guo, and D. L. Fan. Ultrahigh-speed rotating nanoelectromechanical system devices assembled from nanoscale building blocks. *Nature Communications*, 5, apr 2014.

[27] Xiaobin Xu, Kwanoh Kim, and Donglei Fan. Tunable release of multiplex biochemicals by plasmonically active rotary nanomotors. *Angewandte Chemie - International Edition*, 54(8):2525–2529, feb 2015.

[28] Wei Wang, Luz Angelica Castro, Mauricio Hoyos, and Thomas E. Mallouk. Autonomous motion of metallic microrods propelled by ultrasound. *ACS Nano*, 6(7):6122–6132, jul 2012.

[29] Daniel Kagan, Michael J. Benchimol, Jonathan C. Claussen, Erdembileg Chuluun-Erdene, Sadik Esener, and Joseph Wang. Acoustic droplet vaporization and propulsion of perfluorocarbon-loaded microbullets for targeted tissue penetration and deformation. *Angewandte Chemie - International Edition*, 51(30):7519–7522, jul 2012.

[30] Zhiguang Wu, Tianlong Li, Jinxing Li, Wei Gao, Tailin Xu, Caleb Christianson, Weiwei Gao, Michael Galarnyk, Qiang He, Liangfang Zhang, and Joseph Wang. Turning erythrocytes into functional micromotors. *ACS Nano*, 8(12):12041–12048, dec 2014.

[31] John F. Schenck. Safety of strong, static magnetic fields. *Journal of Magnetic Resonance Imaging*, 12(1):2–19, 2000.

[32] Yu Gu, Ruslan Burtovyy, John Custer, Igor Luzinov, and Konstantin G. Kornev. A gradient field defeats the inherent repulsion between magnetic nanorods. *Royal Society Open Science*, 1(2), oct 2014.

[33] Rémi Dreyfus, Jean Baudry, Marcus L. Roper, Marc Fermigier, Howard A. Stone, and Jérôme Bibette. Microscopic artificial swimmers. *Nature*, 437(7060):862–865, oct 2005.

[34] Famin Qiu, Satoshi Fujita, Rami Mhanna, Li Zhang, Benjamin R. Simona, and Bradley J. Nelson. Magnetic Helical Microswimmers Functionalized with Lipoplexes for Targeted Gene Delivery. *Advanced Functional Materials*, 25(11):1666–1671, jan 2015.

[35] Steven Floyd, Chytra Pawashe, and Metin Sitti. An Untethered Magnetically Actuated Micro-Robot Capable of Motion on Arbitrary Surfaces. Technical report.

[36] Chytra Pawashe, Steven Floyd, and Metin Sitti. Modeling and experimental characterization of an untethered magnetic micro-robot. *International Journal of Robotics Research*, 28(8):1077–1094, aug 2009.

[37] Max T. Hou, Hui Mei Shen, Guan Lin Jiang, Chiang Ni Lu, I. Jen Hsu, and J. Andrew Yeh. A rolling locomotion method for untethered magnetic microrobots. *Applied Physics Letters*, 96(2), 2010.

[38] Guan Lin Jiang, Yunn Horng Guu, Chiang Ni Lu, Pei Kao Li, Hui Mei Shen, Lung Sheng Lee, Jerliang Andrew Yeh, and Max Ti Kuang Hou. Development of rolling magnetic Microrobots. *Journal of Micromechanics and Microengineering*, 20(8), aug 2010.

[39] Roel Pieters, Hsi Wen Tung, Samuel Charreyron, David F. Sargent, and Bradley J. Nelson. RodBot: A rolling microrobot for micromanipulation. *Proceedings - IEEE International Conference on Robotics and Automation*, 2015-June(June):4042–4047, jun 2015.

[40] Dominic R FRUTIGER Dipl Masch-Ing and Eth Zurich. MagMites: Design, Fabrication, and Control of Wireless Resonant Magnetic Micromachines for Dry and Wet Environments. Technical report, 1976.

[41] Dominic Roman Frutiger, Eth Zurich, Brad Nelson, Dominic R Frutiger, Karl Vollmers, Bradley E Kratochvil, and Bradley J Nelson. Small, Fast, and Under Control: Wireless Resonant Magnetic Micro-agents Magnetic MEMS View project Crystal harvesting View project Small, Fast, and Under Control: Wireless Resonant Magnetic Micro-agents. *Article in The International Journal of Robotics Research The International Journal of Robotics Research*, 00(00):0–0, 2010.

[42] Hsi-Wen Tung, Massimo Maffioli, Dominic R. Frutiger, Kartik M. Sivaraman, Salvador Pane, and Bradley J. Nelson. Polymer-based Wireless Resonant Magnetic microrobots. *IEEE Transactions on Robotics*, 30(1):26–32, feb 2014.

[43] Wenqi Hu, Guo Zhan Lum, Massimo Mastrangeli, and Metin Sitti. Small-scale soft-bodied robot with multimodal locomotion. *Nature*, 554(7690):81–85, feb 2018.

[44] Timothy G. Leong, Christina L. Randall, Bryan R. Benson, Noy Bassik, George M. Stern, and David H. Gracias. Tetherless thermobiochemically actuated microgrippers. *Proceedings of the National Academy of Sciences of the United States of America*, 106(3):703–708, jan 2009.

[45] Berta Esteban-Fernández De Ávila, Chava Angell, Fernando Soto, Miguel Angel Lopez-Ramirez, Daniela F. Báez, Sibai Xie, Joseph Wang, and Yi Chen. Acoustically Propelled Nanomotors for Intracellular siRNA Delivery. *ACS Nano*, 10(5):4997–5005, may 2016.

[46] Malthe Hansen-Bruhn, Berta Esteban Fernández de Ávila, Mara Beltrán-Gastélum, Jing Zhao, Doris E. Ramírez-Herrera, Pavimol Angsantikul, Kurt Vesterager Gothelf, Liangfang Zhang, and Joseph Wang. Active Intracellular Delivery of a Cas9/sgRNA Complex Using Ultrasound-Propelled Nanomotors. *Angewandte Chemie - International Edition*, 57(10):2657–2661, mar 2018.

[47] Hao Li, Gwangjun Go, Seong Yong Ko, Jong Oh Park, and Sukho Park. Magnetic actuated pH-responsive hydrogel-based soft micro-robot for targeted drug delivery. *Smart Materials and Structures*, 25(2), jan 2016.

[48] Fei Peng, Yingfeng Tu, Jan C.M. Van Hest, and Daniela A. Wilson. Self-Guided Supramolecular Cargo-Loaded Nanomotors with Chemotactic Behavior towards Cells. *Angewandte Chemie - International Edition*, 54(40):11662–11665, sep 2015.

[49] Victor Garcia-Gradilla, Sirilak Sattayasamitsathit, Fernando Soto, Filiz Kuralay, Ceren Yardimci, Devan Wiitala, Michael Galarnyk, and Joseph Wang. Ultrasound-propelled nanoporous gold wire for efficient drug loading and release. *Small*, 10(20):4154–4159, oct 2014.

[50] Rami Mhanna, Famin Qiu, Li Zhang, Yun Ding, Kaori Sugihara, Marcy Zenobi-Wong, and Bradley J. Nelson. Artificial bacterial flagella for remote-controlled targeted single-cell drug delivery. *Small*, 10(10):1953–1957, may 2014.

[51] Haifeng Xu, Mariana Medina-Sánchez, Veronika Magdanz, Lukas Schwarz, Franziska Hebenstreit, and Oliver G. Schmidt. Sperm-Hybrid Micromotor for Targeted Drug Delivery. *ACS Nano*, 12(1):327–337, jan 2018.

[52] Berta Esteban Fernández De Ávila, Pavimol Angsantikul, Jinxing Li, Miguel Angel Lopez-Ramirez, Doris E. Ramírez-Herrera, Soracha Thamphiwatana, Chuanrui Chen, Jorge Delezuk, Richard Samakapiruk, Valentin Ramez, Liangfang Zhang, and Joseph Wang. Micromotor-enabled active drug delivery for in vivo treatment of stomach infection. *Nature Communications*, 8(1), dec 2017.

[53] Songzhi Xie, Long Zhao, Xiaojie Song, Maosheng Tang, Chuanfei Mo, and Xiaohong Li. Doxorubicin-conjugated Escherichia coli Nissle 1917 swimmers to achieve tumor targeting and responsive drug release. *Journal of controlled release : official journal of the Controlled Release Society*, 268:390–399, dec 2017.

[54] Jingwei Xue, Zekai Zhao, Lei Zhang, Lingjing Xue, Shiyang Shen, Yajing Wen, Zhuoyuan Wei, Lu Wang, Lingyi Kong, Hongbin Sun, Qineng Ping, Ran Mo, and Can Zhang. Neutrophil-mediated anticancer drug delivery for suppression of postoperative malignant glioma recurrence. *Nature nanotechnology*, 12(7):692–700, 2017.

[55] Xiaohui Yan, Qi Zhou, Melissa Vincent, Yan Deng, Jiangfan Yu, Jianbin Xu, Tiantian Xu, Tao Tang, Liming Bian, Yi Xiang J. Wang, Kostas Kostarelos, and Li Zhang. Multifunctional biohybrid magnetite microrobots for imaging-guided therapy. *Science Robotics*, 2(12), nov 2017.

[56] Hakan Ceylan, I. Ceren Yasa, Oncay Yasa, A. Fatih Tabak, Joshua Giltinan, and Metin Sitti. 3D-Printed Biodegradable Microswimmer for Drug Delivery and Targeted Cell Labeling. *bioRxiv*, page 379024, jul 2018.

[57] S. Shinkai T. D. James, M. D. Phillips. *Boronic Acids in Saccharide Recognition*. Royal Society of Chemistry, 2006.

[58] Yunjie Li, Xiaoxiao Hu, Ding Ding, Yuxiu Zou, Yiting Xu, Xuewei Wang, Yin Zhang, Long Chen, Zhuo Chen, and Weihong Tan. In situ targeted MRI detection of Helicobacter pylori with stable magnetic graphitic nanocapsules. *Nature Communications*, 8(1):15653, aug 2017.

[59] Diana Vilela, Unai Cossío, Jemish Parmar, Angel M. Martínez-Villacorta, Vanessa Gómez-Vallejo, Jordi Llop, and Samuel Sánchez. Medical Imaging for the Tracking of Micromotors. *ACS Nano*, 12(2):1220–1227, feb 2018.

[60] Alexander A. Solovev, Wang Xi, David H. Gracias, Stefan M. Harazim, Christoph Deneke, Samuel Sanchez, and Oliver G. Schmidt. Self-propelled nanotools. *ACS Nano*, 6(2):1751–1756, feb 2012.

[61] Wang Xi, Alexander A. Solovev, Adithya N. Ananth, David H. Gracias, Samuel Sanchez, and Oliver G. Schmidt. Rolled-up magnetic microdrillers: Towards remotely controlled minimally invasive surgery. *Nanoscale*, 5(4):1294–1297, feb 2013.

[62] Kate Malachowski, Mustapha Jamal, Qianru Jin, Beril Polat, Christopher J. Morris, and David H. Gracias. Self-folding single cell grippers. In *Food, Pharmaceutical and Bioengineering Division 2015 - Core Programming Area at the 2015 AIChE Meeting*, volume 1, pages 104–110. AIChE, 2015.

[63] Tonguc O. Tasci, Dante Disharoon, Rogier M. Schoeman, Kuldeepsinh Rana, Paco S. Herson, David W.M. Marr, and Keith B. Neeves. Enhanced Fibrinolysis with Magnetically Powered Colloidal Microwheels. *Small*, 13(36), sep 2017.

[64] Maria Guix, Jahir Orozco, Miguel Garcia, Wei Gao, Sirilak Sattayasamitsathit, Arben Merkoči, Alberto Escarpa, and Joseph Wang. Superhydrophobic alkanethiol-coated microsubmarines for effective removal of oil. *ACS Nano*, 6(5):4445–4451, may 2012.

[65] Zhiguang Wu, Tianlong Li, Wei Gao, Tailin Xu, Beatriz Jurado-Sánchez, Jinxing Li, Weiwei Gao, Qiang He, Liangfang Zhang, and Joseph Wang. Cell-Membrane-Coated Synthetic Nanomotors for Effective Biodetoxification. *Advanced Functional Materials*, 25(25):3881–3887, jul 2015.

[66] Jinxing Li, Pavimol Angsantikul, Wenjuan Liu, Berta Esteban-Fernández de Ávila, Xiaocong Chang, Elodie Sandraz, Yuyan Liang, Siyu Zhu, Yue Zhang, Chuanrui Chen, Weiwei Gao, Liangfang Zhang, and Joseph Wang. Biomimetic Platelet-Camouflaged Nanorobots for Binding and Isolation of Biological Threats. *Advanced Materials*, 30(2), jan 2018.

[67] Susana Campuzano, Jahir Orozco, Daniel Kagan, Maria Guix, Wei Gao, Sirilak Sattayasamitsathit, Jonathan C. Claussen, Arben Merkoçi, and Joseph Wang. Bacterial isolation by lectin-modified microengines. *Nano Letters*, 12(1):396–401, jan 2012.

[68] Victor Garcia-Gradilla, Jahir Orozco, Sirilak Sattayasamitsathit, Fernando Soto, Filiz Kuralay, Ashley Pourazary, Adlai Katzenberg, Wei Gao, Yufeng Shen, and Joseph Wang. Functionalized ultrasound-propelled magnetically guided nanomotors: Toward practical biomedical applications. *ACS Nano*, 7(10):9232–9240, oct 2013.

[69] Yabin Zhang, Kai Yan, Fengtong Ji, and Li Zhang. Enhanced Removal of Toxic Heavy Metals Using Swarming Biohybrid Adsorbents. *Advanced Functional Materials*, 28(52), dec 2018.

[70] B. Jurado-Sánchez, A. Escarpa, and J. Wang. Lighting up micromotors with quantum dots for smart chemical sensing. *Chemical Communications*, 51(74):14088–14091, jul 2015.

[71] Limei Liu, Yonggang Dong, Yunyu Sun, Mei Liu, Yajun Su, Hui Zhang, and Bin Dong. Motion-based pH sensing using spindle-like micromotors. *Nano Research*, 9(5):1310–1318, may 2016.

[72] Chenghao Bi, Maria Guix, Benjamin V Johnson, Wuming Jing, and David J Cappelleri. Design of microscale magnetic tumbling robots for locomotion in multiple environments and complex terrains. *Micromachines*, 9(2):1–17, feb 2018.

[73] Wuming Jing, Nicholas Pagano, and David J Cappelleri. A MICRO-SCALE MAGNETIC TUMBLING MICROROBOT. Technical report, 2012.

[74] Wuming Jing, Nicholas Pagano, and David J. Cappelleri. A tumbling magnetic microrobot with flexible operating modes. *Proceedings - IEEE International Conference on Robotics and Automation*, pages 5514–5519, 2013.

[75] Juha Pyrhonen, Tapani Jokinen, and Valeria Hrabovcova. *Design of Rotating Electrical Machines, 2nd Edition -*. 2013.

[76] Hill Technical Sales. Amorphous Magnetic Cores, 2005.

[77] C. Bi, E. Niedert, G. Adam, E. Lambert, L. Solorio, C. Goergen, and D. Cappelleri. Tumbling Magnetic Microrobots for Biomedical Applications. *IEEE International Conference on Robotics, Manipulation, and Automation at Small Scales (MARSS)*, 2019.

[78] Jiayin Xie, Chenghao Bi, David J. Cappelleri, and Nilanjan Chakraborty. Towards Dynamic Simulation Guided Optimal Design of Tumbling Microrobots. jul 2019.

[79] C Pawashe, S Floyd, and M Sitti. Dynamic modeling of stick slip motion in an untethered magnetic microrobot. *Robotics: Science and Systems IV, Zurich, Switzerland*, 2008.

[80] Jiayin Xie and Nilanjan Chakraborty. Rigid body dynamic simulation with line and surface contact. In *IEEE International Conference on Simulation, Modeling, and Programming for Autonomous Robots (SIMPAR)*, pages 9–15, 2016.

[81] Jiayin Xie and Nilanjan Chakraborty. Rigid Body Dynamic Simulation With Multiple Convex Contact Patches. In *ASME 2018 IDETC*, pages V006T09A002—-V006T09A002, 2018.

[82] Jiayin Xie and Nilanjan Chakraborty. Rigid Body Motion Prediction with Planar Non-convex Contact Patch. In *IEEE International Conference on Robotics and Automation (ICRA)*, 2019.

[83] Per Lotstedt. Mechanical Systems of Rigid Bodies Subject to Unilateral Constraints. *SIAM Journal on Applied Mathematics*, 42(2):281–296, 1982.

[84] M Anitescu, J F Cremer, and F A Potra. Formulating 3D Contact Dynamics Problems. *Mechanics of Structures and Machines*, 24(4):405–437, 1996.

[85] Jong-Shi Pang and Jeffrey C Trinkle. Complementarity formulations and existence of solutions of dynamic multi-rigid-body contact problems with Coulomb friction. *Mathematical programming*, 73(2):199–226, 1996.

[86] David E Stewart and Jeffrey C Trinkle. An implicit time-stepping scheme for rigid body dynamics with inelastic collisions and coulomb friction. *International Journal for Numerical Methods in Engineering*, 39(15):2673–2691, 1996.

[87] Evan Drumwright and Dylan A Shell. Extensive analysis of Linear Complementarity Problem (LCP) solver performance on randomly generated rigid body contact problems. In *Proceedings of the IEEE/RSJ International Conference on Intelligent Robots and Systems (IROS)*, pages 5034–5039, oct 2012.

[88] Emanuel Todorov. Convex and analytically-invertible dynamics with contacts and constraints: Theory and implementation in MuJoCo. In *Proceedings of the IEEE International Conference on Robotics and Automation (ICRA)*, pages 6054–6061, may 2014.

[89] Mihai Anitescu and Florian A Potra. Formulating dynamic multi-rigid-body contact problems with friction as solvable linear complementarity problems. *Nonlinear Dynamics*, 14(3):231–247, 1997.

[90] Mihai Anitescu and Florian A Potra. A time-stepping method for stiff multibody dynamics with contact and friction. *International Journal for Numerical Methods in Engineering*, 55(7):753–784, 2002.

[91] James E Tzitzouris. *Numerical Resolution of Frictional Multi-Rigid-Body Systems via Fully Implicit Time-Stepping and Nonlinear Complementarity*. PhD thesis, Johns Hopkins University, 2001.

[92] Nilanjan Chakraborty, Stephen Berard, Srinivas Akella, and Jeffrey C Trinkle. A geometrically implicit time-stepping method for multibody systems with intermittent contact. *The International Journal of Robotics Research*, 33(3):426–445, 2014.

[93] Michael Erdmann. On a representation of friction in configuration space. *The International Journal of Robotics Research*, 13(3):240–271, 1994.

[94] Suresh Goyal, Andy Ruina, and Jim Papadopoulos. Planar sliding with dry friction part 1. limit surface and moment function. *Wear*, 143(2):307–330, 1991.

[95] Robert D Howe and Mark R Cutkosky. Practical force-motion models for sliding manipulation. *The International Journal of Robotics Research*, 15(6):557–572, 1996.

[96] Richard M Murray, Zexiang Li, and S Shankar Sastry. *An Mathematical Introduction to Robotic Manipulation*. CRC Press, Boca Raton, FL, 1994.

[97] R S Fearing. Survey of sticking effects for micro parts handling. In *IEEE/RSJ International Conference on Intelligent Robots and Systems. Human Robot Interaction and Cooperative Robots*, volume 2, pages 212–217 vol.2, aug 1995.

[98] Jean J Moreau. Unilateral contact and dry friction in finite freedom dynamics. In *Nonsmooth Mechanics and Applications*, pages 1–82. Springer, 1988.

[99] Ingrid Ordás, Lars Eckmann, Mark Talamini, Daniel C Baumgart, and William J Sandborn. Ulcerative colitis. *The Lancet*, 380(9853):1606–1619, 2012.

[100] M J Denters, M Schreuder, A C Depla, R C Mallant-Hent, M C A van Kouwen, M Deutekom, P M Bossuyt, P Fockens, and E den Dekker. Patients' perception of colonoscopy: patients with inflammatory bowel disease and irritable bowel syndrome experience the largest burden. *European Journal of Gastroenterology & Hepatology*, 25:964–972, 2013.

[101] Stacy Menees, Peter Higgins, Sheryl Korsnes, and Grace Elta. Does colonoscopy cause increased ulcerative colitis symptoms? *Inflammatory Bowel Diseases*, 13(1):12–18, 2007.

[102] Tomohiro Ogawa, Yoshio Ohda, Kazuko Nagase, Tomoaki Kono, Katsuyuki Tozawa, Toshihiko Tomita, Masaki Iimuro, Nobuyuki Hida, Tadayuki Oshima, Hirokazu Fukui, Kazutoshi Hori, Jiro Watari, Shiro Nakamura, and Hiroto Miwa. Evaluation of discomfort during colonoscopy with conventional and ultrathin colonoscopes in ulcerative colitis patients. *Digestive Endoscopy*, 27(1):99–105, 2015.

[103] Fabrizio Parente, Mirko Molteni, Barbara Marino, Agostino Colli, Sandro Ardizzone, Salvatore Greco, Gianluca Sampietro, Diego Foschi, and Silvano Gallus. Are colonoscopy and bowel ultrasound useful for assessing response to short-term therapy and predicting disease outcome of moderate-to-severe forms of ulcerative colitis: A prospective study. *American Journal of Gastroenterology*, 105(5):1150–1157, 2010.

[104] Shiho Takashima, Jun Kato, Sakiko Hiraoka, Asuka Nakarai, Daisuke Takei, Toshihiro Inokuchi, Yuusaku Sugihara, Masahiro Takahara, Keita Harada, Hiroyuki Okada, Takehiro Tanaka, and Kazuhide Yamamoto. Evaluation of mucosal healing in ulcerative colitis by fecal calprotectin vs. fecal immunochemical test. *American Journal of Gastroenterology*, 110(6):873–880, 2015.

[105] David Halliday, Robert Resnick, and Jearl Walker. *Fundamentals of Physics*. John Wiley & Sons, Inc., Hoboken, 9 edition, 2011.

[106] Juan Manuel Camacho and Victor Sosa. Alternative method to calculate the magnetic field of permanent magnets with azimuthal symmetry. *Revista mexicana de física E*, 59:8–17, 2013.

[107] Jessica L. Freeling and Khosrow Rezvani. Assessment of murine colorectal cancer by micro-ultrasound using three dimensional reconstruction and non-linear contrast imaging. *Molecular Therapy - Methods and Clinical Development*, 3(July):16070, 2016.

[108] Thomas Heinar. Medical gel. *United States Patent and Trademark Office, 2013.*

[109] Jessica L. Freeling and Khosrow Rezvani. Assessment of murine colorectal cancer by micro-ultrasound using three dimensional reconstruction and non-linear contrast imaging. *Molecular Therapy - Methods and Clinical Development*, 3:16070, mar 2016.

[110] Shin-Etsu. Tylose for Personal Care. *SE Tylose GmbH & Co.,* 2018.

[111] Mehdi Modabberifar and Matthew Spenko. A shape memory alloy-actuated gecko-inspired robotic gripper. *Sensors and Actuators, A: Physical*, 276:76–82, jun 2018.

[112] Soichiro Tottori, Naohiko Sugita, Reo Kometani, Sunao Ishihara, and Mamoru Mitsuishi. Selective control method for multiple magnetic helical microrobots. *Journal of Micro-Nano Mechatronics*, 6(3-4):89–95, jun 2011.

[113] Sagar Chowdhury, Wuming Jing, and David J. Cappelleri. Towards independent control of multiple magnetic mobile microrobots. *Micromachines*, 7(1):1–14, 2016.